Chapter 5

A MECHANISTIC STUDY OF THE OXIDATIVE REACTION OF HYDROGEN-TERMINATED Si(111) SURFACES WITH LIQUID METHANOL

Plymale, N. T.; Dasog, M.; Brunschwig, B. S.; Lewis, N. S. A Mechanistic Study of the Oxidative Reaction of Hydrogen-Terminated Si(111) Surfaces with Liquid Methanol, *in preparation.*

5.1 INTRODUCTION

The device properties of Si can be manipulated through control over the structure and chemical composition of crystalline Si surfaces.[1-2] The reactivity of hydrogen-terminated Si(111) (H–Si(111)) surfaces toward organic nucleophiles, including alkenes,[3-4] alkynes,[5-6] amines,[7-11] thiols and disulfides,[12-13] Grignards,[14-15] and alcohols,[16-25] has been widely exploited to impart desirable functionality to the Si interface. These surface reactions have been used to control the interface between Si and metals,[26-31] metal oxides,[32-35] polymers,[36-41] and redox assemblies.[42-49]

Many nucleophiles react with H–Si(111) surfaces under mild conditions[50-51] compared to analogous reactions with molecular silanes. For example, the reaction of H–Si(111) surfaces with alcohols has no analogous molecular counterpart.[52,18] The unique reactivity of H–Si(111) surfaces with alcohols, including CH_3OH, has been exploited as a versatile method to impart a desired functionality to the surface via the robust Si–O bond,

without the formation of thick insulating silicon oxide layers on the surface. For example, n-Si/CH_3OH junctions have yielded high open-circuit voltages (632–640 mV) and high device efficiencies (12–14%)[53-54] in regenerative photoelectrochemical cells, with the device performance correlated with low surface recombination velocities[55-57] as well as the favorable band-edge positions[58] of the methoxylated Si surface. The methoxy termination can moreover be converted to F-termination or OH-termination,[19, 24] both of which are synthetically difficult to achieve otherwise on Si(111) surfaces.

Small molecule silanes that model the H–Si(111) surface, such as tris(trimethylsilyl)silane (TTMSS), are generally good models for radical reactions at H–Si(111) surfaces because the Si–H bond strength is comparable for both systems.[59] In the presence of CH_3OH, however, TTMSS decomposes by Si–Si bond cleavage.[52, 60] Similarly, the Si–Si bonds on H-terminated nanoporous Si surfaces cleave by thermal reaction with alcohols.[52, 61] In contrast, the H–Si(111) surface primarily undergoes a substitution reaction with alcohols, resulting in ≡Si–OR functionality on the surface. Scanning-tunneling microscopy (STM) data have demonstrated that the H–Si(111) surface undergoes microscopic etching after 30 min in warm (65 °C) CH_3OH, but methoxylated H–Si(111) sites are effectively passivated toward etching.[62]

The electronic structure of crystalline Si, which differs significantly from that of model silanes, is often invoked to understand reactions that take place exclusively on H–Si(111) surfaces. Reactions that involve electron transfer at the H–Si(111) surface, such as the reaction of H–Si(111) surfaces with alcohols, are good candidate reactions to elucidate the role of the Si electronic structure in surface reactions. The general

understanding of the alkoxylation mechanism has been focused primarily on a qualitative discussion that implicates the narrow band gap of bulk Si in supporting more electronic states than can be supported by analogous molecular silanes. These mechanisms shown in Schemes 5.1,[21] 5.2;[18] provide a description of the chemical transformations that take place during surface alkoxylation, but the electronic rearrangements during these reactions are not yet clearly elaborated. Elucidating the mechanism of the reaction of H–Si(111) surfaces with CH_3OH in the presence of a series of oxidants offers a unique opportunity to determine the role of the Si electronic structure in the surface reaction.

Scheme 5.1. Methoxylation of H–Si(111) Surfaces in the Absence of an Oxidant[21]

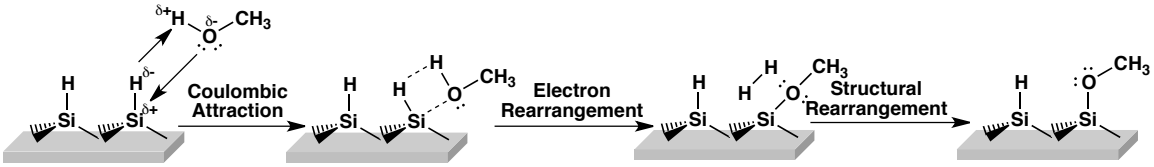

Scheme 5.2. Oxidant-Activated Methoxylation of H–Si(111)[17-18]

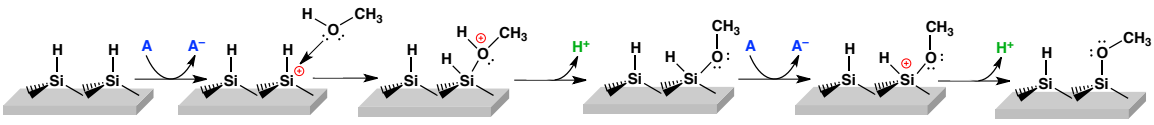

Herein we characterize the reaction of H–Si(111) surfaces with CH_3OH in the absence or presence of an oxidant species and in the absence or presence of illumination. We have elucidated the dependence of the methoxylation reaction on the formal potential of the oxidant. Additionally, we have delineated the roles of the electronic surface states and bulk Si band structure in the electron transfer processes that are involved in the methoxylation reaction. A general mechanism by which the reaction of H–Si(111) surfaces with CH_3OH takes place under the conditions studied is proposed in the context of conventional charge transfer kinetics at the semiconductor interface.

5.2 EXPERIMENTAL SECTION

5.2.1 Materials and Methods

Water (≥18.2 MΩ cm resistivity) was obtained from a Barnstead E-Pure system. Aqueous ammonium fluoride (NH_4F(aq), 40% semiconductor grade, Transene Co. Inc., Danvers MA) was deaerated by bubbling with Ar(g) (99.999%, Air Liquide) for ≥1 h prior to use. Methanol (CH_3OH, anhydrous, ≥99.8%, Sigma-Aldrich) was used as received. Float-zone-grown, phosphorus-doped n-Si(111) "intrinsic" wafers (University Wafer, Boston, MA) were double-side polished, 525 ± 15 μm thick, oriented within 0.5° of the (111) crystal plane, and had a resistivity of 2.0 kΩ cm. Czochralski-grown, phosphorus-doped n-Si(111) wafers (Virginia Semiconductor, Fredericksburg, VA) were double-side polished, 381 ± 25 μm thick, oriented within 0.1° of the (111) crystal plane, and had a resistivity of 1.0 Ω cm. Czochralski-grown, boron-doped p-Si(111) wafers

(Addison Engineering, San Jose, CA) were double-side polished, 300 ± 25 μm thick, oriented within 0.5° of the (111) crystal plane, and had a resistivity of 0.40 Ω cm.

The dopant densities (N_d) were determined from the resistivities for each Si substrate. For intrinsic Si(111), $N_d = 2.2 \times 10^{12}$ cm^{-3}; for n-type Si(111), $N_d = 4.9 \times 10^{15}$ cm^{-3}; and for p-type Si(111), $N_d = 4.2 \times 10^{16}$ cm^{-3}. The positions of the n-type and p-type Si(111) bulk Fermi levels ($\mathbf{E}_{F,n,b}$ and $\mathbf{E}_{F,p,b}$, respectively) were determined using eq 5.1 and eq 5.2 for each of the dopant concentrations used.

$$\mathbf{E}_{F,n,b} = \mathbf{E}_{cb} + k_B T \ln\left(\frac{N_d}{N_C}\right) \qquad (5.1)$$

$$\mathbf{E}_{F,p,b} = \mathbf{E}_{vb} - k_B T \ln\left(\frac{N_d}{N_C}\right) \qquad (5.2)$$

$\mathbf{E}_{cb}$ and $\mathbf{E}_{vb}$ are the energy positions of the Si conduction band minimum (–4.05 eV vs $\mathbf{E}_{Vac}$) and Si valence band maximum (–5.17 eV vs $\mathbf{E}_{Vac}$),[63] respectively, k_B is the Boltzmann constant, T is the temperature in Kelvin (296 K), q is the absolute value of the elementary charge, N_C is the effective density of states of the Si conduction band (2.8×10^{19} cm^{-3}), and N_V is the effective density of states of the Si valence band (1.0×10^{19} cm^{-3}). The bulk Fermi level of intrinsic Si(111) ($\mathbf{E}_{F,i,b}$), which was lightly n-type, was determined using eq 5.1.

1. Preparation and Purification of the Oxidants. 1,1'-dimethylferrocenium ($Me_2Cp_2Fe^+BF_4^-$, bis(methylcyclopentadienly)iron(III) tetrafluoroborate), octamethyl-ferrocenium ($Me_8Cp_2Fe^+BF_4^-$, bis(tetramethylcyclopentadienyl)iron(III) tetrafluoro-borate), and decamethylferrocenium ($Cp^*_2Fe^+BF_4^-$, bis(pentamethylcyclopentadienyl)-iron(III) tetrafluoroborate) were prepared by chemical oxidation of the neutral

metallocenes[64-65] 1,1'-dimethylferrocene (Me_2Cp_2Fe, bis(methylcyclopentadienyl)iron(II), 95%, Sigma-Aldrich), octamethylferrocene (Me_8Cp_2Fe, bis(tetramethylcyclopentadienyl)iron(II), 98%, Strem Chemical), and decamethylferrocene (Cp^*_2Fe, bis(pentamethylcyclopentadienyl)iron(II), 99%, Strem Chemical), respectively. Ferrocenium ($Cp_2Fe^+BF_4^-$, bis(cyclopentadienyl)iron(III) tetrafluoroborate, technical grade, Sigma-Aldrich) $Me_2Cp_2Fe^+BF_4^-$, $Me_8Cp_2Fe^+BF_4^-$, and $Cp^*_2Fe^+BF_4^-$ were purified by recrystallization from diethyl ether (inhibitor-free, ≥99.9% Sigma-Aldrich) and CH_3CN (anhydrous, ≥99.8% Sigma-Aldrich). Methyl viologen ($MV^{2+}(Cl^-)_2$, 1,1'-dimethyl-4,4'-bipyridinium dichloride hydrate, 98%, Sigma-Aldrich) and cobaltocenium ($Cp_2Co^+PF_6^-$, bis(cyclopentadienyl)cobalt(III) hexafluorophosphate, 98%, Sigma-Aldrich) were recrystallized from ethanol (anhydrous, ≥99.5% Sigma-Aldrich) prior to use. Acetylferrocenium ($(CpCOCH_3)CpFe^+$, (acetylcyclopentadienyl)cyclopentadienyliron(III)) was generated in CH_3OH containing 1.0 M $LiClO_4$ (battery grade, Sigma-Aldrich) from acetylferrocene ($(CpCOCH_3)CpFe$, acetylcyclopentadienyl)cyclopentadienyliron(II), Sigma-Aldrich, purified by sublimation) by controlled-potential electrolysis at a Pt mesh working electrode with a Pt mesh counter electrode located in a compartment separated from the working electrode by a Vycor frit.[65] The electrolysis was performed at +0.5 V vs a Pt pseudo-reference electrode, and sufficient current was passed to generate 1.0 mM $(CpCOCH_3)CpFe^+$ from 10 mM $(CpCOCH_3)CpFe$. The $(CpCOCH_3)CpFe^+$ was used within 1 min of its generation.

2. Preparation of H–Si(111) Surfaces. Si wafers were scored and broken to the desired size using a diamond- or carbide-tipped scribe. The Si surfaces were rinsed

sequentially with water, methanol (≥99.8%, BDH), acetone (≥99.5%, BDH), methanol, and water. The samples were oxidized in a piranha solution (1:3 v/v of 30% H_2O_2(aq) (EMD): 18 M H_2SO_4(aq) (EMD)) for 10–15 min at 95 ± 5 °C. The wafers were removed, rinsed with copious amounts of water, and immersed in buffered hydrofluoric acid(aq) (BHF, semiconductor grade, Transene Co. Inc.) for 18 s. The BHF solution was drained and the wafers were rinsed with H_2O. Anisotropic etching was then performed in an Ar(g)-purged solution of 40% NH_4F(aq) for 5.5 min for wafers having a 0.5° miscut angle, and for 9.0 min for wafers having a 0.1° miscut angle.[66] The wafers were removed, rinsed with H_2O, and dried under a stream of Ar(g).

3. Methoxylation of H–Si(111) Surfaces. The H–Si(111) wafers were transferred to a N_2(g)-purged glovebox (<10 ppm O_2(g)) and immersed in either neat CH_3OH or in a solution of CH_3OH that contained 1.0 mM of $(CpCOCH_3)CpFe^+$, $Cp_2Fe^+BF_4^-$, $Me_2Cp_2Fe^+BF_4^-$, $Me_8Cp_2Fe^+BF_4^-$, $Cp^*_2Fe^+BF_4^-$, $MV^{2+}2Cl^-$, or $Cp_2Co^+PF_6^-$. Reactions in the dark were performed in test tubes wrapped in black vinyl electrical tape with the top covered in Al foil, whereas reactions in the light were performed under ambient illumination. Upon completion of the reaction, the wafers were removed from the CH_3OH solution and rinsed sequentially with CH_3OH and tetrahydrofuran (THF, anhydrous, ≥99.9%, Sigma-Aldrich). The THF was allowed to evaporate and the samples were removed from the glovebox. Prior to analysis, the wafers were rinsed briefly with H_2O and dried under a stream of Ar(g).

4. Potentiostatic Methoxylation of H–Si(111). Si samples were cleaned using a piranha solution for 10 min at 95 ± 5 °C and etched in BHF for 18 s prior to electrode

fabrication. Ohmic contacts to the back of n-Si(111) (1.0 Ω cm) electrodes were made by using a diamond-tipped scribe to apply Ga-In eutectic (78% Ga, 22% In by weight). Ohmic contacts to the back of p-Si(111) (0.40 Ω cm) electrodes were made by electron-beam evaporation (Denton Vacuum) of 100 nm of Al to the rear face of the electrode, followed by a 30 min anneal under forming gas (5% H_2(g) in N_2(g)) at 450 °C.[67] Using high-purity conductive Ag paint (SPI supplies, West Chester, PA), the Si working electrodes were adhered to a coil of tinned Cu wire that had been threaded through 1/4" outer diameter Pyrex tubing. Loctite 9460 epoxy was used to insulate the rear face of the electrode from the electrolyte as well as to immobilize the Si wafer such that the electrode face was perpendicular to the length of the tubing.[67] The electrode areas (0.2–0.4 cm^2) were measured by analysis of scanned images of the electrodes using ImageJ software.

Immediately prior to performing the electrochemical experiments, the electrodes were immersed in BHF for 18 s, rinsed with water, and dried thoroughly. The electrodes were then immersed in 40% NH_4F(aq), with wafers having a 0.5° miscut angle immersed for 5.5 min whereas wafers that had a 0.1° miscut angle were immersed for 9.0 min. The electrodes were rinsed with water and dried thoroughly prior to performing electrochemical measurements.

Electrochemical measurements were performed in a four-port, cylindrical, flat-bottomed, borosilicate glass cell that contained CH_3OH with 1.0 M $LiClO_4$. Electrochemical measurements were collected using a Solartron 1286 model potentiostat operated by CorrWare software v. 3.2c. Current density vs potential (*J*-*E*) measurements

were collected using a 3-electrode setup with a Si working electrode, a saturated calomel reference electrode (SCE, CH instruments, Inc., Austin TX), and a Pt mesh counter electrode. *J-E* data were collected by sweeping the potential from negative to positive using a scan rate of 50 mV s^{-1} and a sampling rate of 1 mV per data point, with active stirring of the electrolyte. Measurements were performed in the dark as well as under 10 mW cm^{-2} of illumination intensity provided by a 300 W ELH-type W-halogen lamp. The illumination intensity was determined by use of a calibrated Si photodiode (Thor Laboratories, Newton, NJ).

5. Determination of the Oxidant Formal Potentials. The formal potentials of the oxidant species (1.0 mM in CH_3OH) were determined by cyclic voltammetry vs a $Cp_2Fe^{+/0}$ internal reference using Pt wire working and reference electrodes and a Pt mesh counter electrode. The formal potential of the $Cp_2Fe^{+/0}$ couple was measured vs a SCE reference ($E°'(Cp_2Fe^{+/0})$ = 0.325 V vs SCE), and all of the oxidant formal potentials was converted to SCE using this value for the shift in reference potentials.. The supporting electrolyte was 1.0 M $LiClO_4$ for $(CpCOCH_3)CpFe^{+/0}$, $Cp_2Fe^{+/0}$, $Me_2Cp_2Fe^{+/0}$, $Me_8Cp_2Fe^{+/0}$, $Cp^*_2Fe^{+/0}$, and $Cp_2Co^{+/0}$ and was 0.1 M tetrabutylammonium hexafluoro-phosphate ($TBAPF_6$, Sigma-Aldrich) for $MV^{2+/+\bullet}$.

5.2.2 Instrumentation

1. Transmission Infrared Spectroscopy. Transmission infrared spectroscopy (TIRS) was performed using a Thermo Scientific Nicolet 6700 optical spectrometer equipped with an electronically temperature-controlled EverGlo mid-IR source, a KBr beamsplitter, a deuterated L-alanine-doped triglycine sulfate (DLaTGS) detector, and a

N_2(g) purge.[66-67] The samples, cut to ~1.3 × 3.2 cm, were mounted using a custom attachment such that the angle between the path of the beam and the surface normal was 74° (Brewster's angle for Si). The reported spectra are averages of 1500 consecutive scans collected at 4 cm^{-1} resolution. Spectra were referenced to spectrum of either the silicon oxide (SiO_x) or H–Si(111) surface, which were collected separately for each sample. Data were collected and processed using OMNIC software v. 9.2.41. The baseline was flattened and residual water peaks were subtracted to produce the reported spectral data.

2. X-ray Photoelectron Spectroscopy. X-ray photoelectron spectroscopic (XPS) data were collected using a Kratos AXIS Ultra spectrometer equipped with a monochromatic Al Kα X-ray source at 1486.7 eV, a hybrid electrostatic and magnetic lens system, and a delay-line detector.[66-67] Photoelectrons from a 700 μm × 300 μm area were ejected at 90° with respect to the sample surface. Survey and high-resolution spectra were collected with an analyzer pass energy of 80 eV and 10 eV, respectively. The chamber base pressure was ~8 × 10^{-10} Torr. Calibration of the energy scale and work function was performed using clean Au, Ag, and Cu samples. The data were collected using Vision Manager software v. 2.2.10 revision 5.

5.2.3 Analysis of TIRS and XPS Data

1. Calculation of the Methoxy Fractional Monolayer Coverage from TIRS Data. The fractional monolayer (ML) coverage of H–Si(111) sites remaining after reaction in CH_3OH (θ_{Si-H}) was determined using eq 5.3:

$$\theta_{\text{Si–H}} = \frac{A_{\nu(\text{Si–H}),f}}{A_{\nu(\text{Si–H}),i}} \qquad (5.3)$$

$A_{\nu(\text{Si–H}),f}$ and $A_{\nu(\text{Si–H}),i}$ are the final and initial area, respectively, under the Si–H stretching peak. Assuming that all atop sites are terminated by Si–H or Si–OCH_3 groups, the fractional ML coverage of CH_3O–Si(111) sites ($\theta_{\text{Si–OCH}_3}$) was determined using eq 5.4:

$$\theta_{\text{Si–OCH}_3} = 1 - \theta_{\text{Si–H}} \qquad (5.4)$$

2. Calculation of the Methoxy Fractional Monolayer Coverage from XPS Data. High-resolution C 1s and Si 2p XPS data were analyzed using CasaXPS v. 2.3.16. C 1s spectra were fitted using a Voigt GL(30) line function, which consisted of 70% Gaussian and 30% Lorentzian character. Bulk Si 2p data were fitted using a line function of the form LA(*a*, *b*, *n*), where *a* and *b* define the asymmetry of the line shape and *n* defines the Gaussian width. LA(1.2, 1.4, 200) was used in this work. Contributions from SiO_x were fitted using the GL(30) line shape. Spectra were analyzed using a linear background.

A substrate-overlayer model was used to determine the thickness of the methoxy overlayer, $d_{\text{Si–OCH}_3}$, by XPS:

$$\left(\frac{I_{\text{C–O}}}{I_{\text{Si}}}\right)\left(\frac{SF_{\text{Si}}}{SF_{\text{C–O}}}\right)\left(\frac{\rho_{\text{Si}}}{\rho_{\text{C–O}}}\right) = \left(\frac{1 - e^{-\frac{d_{\text{Si–OCH}_3}}{\lambda_{\text{C–O}}\sin\varphi}}}{e^{-\frac{d_{\text{Si–OCH}_3}}{\lambda_{\text{Si}}\sin\varphi}}}\right) \qquad (5.5)$$

$I_{\text{C–O}}$ and I_{Si} are the areas under the photoemission peaks arising from C bound to O and from bulk Si, respectively, $SF_{\text{C–O}}$ and SF_{Si} are the sensitivity factors for the C 1s (0.278) and Si 2p (0.328) photoemission signals, respectively, $\rho_{\text{C–O}}$ and ρ_{Si} are the density of the hydrocarbon overlayer (3.0 g cm^{-3}) and Si (2.3 g cm^{-3}), respectively, $\lambda_{\text{C–O}}$ and λ_{Si} are the attenuation lengths of C 1s photoelectrons (3.6 nm) and Si 2p photoelectrons (4.0 nm),

respectively, moving through a hydrocarbon overlayer, and φ is the angle between the photoelectron ejection vector and the instrument analyzer (90° for this work). The thickness $d_{Si–OCH_3}$ was determined using an iterative process, and $\theta_{Si–OCH_3}$ was calculated by dividing by the estimated thickness of 1 ML of methoxy groups (0.20 nm).

Some samples exhibited the presence of F by XPS. The fractional monolayer coverage of F^- was calculated from high-resolution XPS data using eq 5.6.

$$\left(\frac{I_{\mathrm{F\ 1s}}}{I_{\mathrm{Si}}}\right)\left(\frac{SF_{\mathrm{Si}}}{SF_{\mathrm{F\ 1s}}}\right)\left(\frac{\rho_{\mathrm{Si}}}{\rho_{\mathrm{O}}}\right)=\left(\frac{1-e^{\frac{d_{\mathrm{F}}}{\lambda_{\mathrm{F}}\sin\varphi}}}{e^{\frac{d_{\mathrm{F}}}{\lambda_{\mathrm{Si}}\sin\varphi}}}\right) \qquad (5.6)$$

$I_{\mathrm{F\ 1s}}$ is the area under the F 1s photoemission peak (both peaks present in Figure 5.9), $SF_{\mathrm{F\ 1s}}$ is the sensitivity factor for the F 1s photoemission signal (1.00), ρ_{O} is the density of the terminating overlayer (assumed to be primarily hydrocarbon, giving ρ_{S} = 3.0 g cm^{-3}), and λ_{F} is the attenuation length of F 1s photoelectrons moving through a halogen overlayer (1.6 nm).[18] The remaining terms in eq 5.6 are defined for eq 5.5. The thickness of the F layer d_{F} was determined using an iterative process, and the fractional monolayer coverage of F, θ_{F}, was calculated by dividing by the estimated thickness of 1 ML of F^- ion (0.13 nm).[67]

5.3 RESULTS

5.3.1 Reaction of H–Si(111) with CH_3OH Solutions in the Dark

Figure 5.1 presents time dependence for the dark reaction of H–Si(111) surfaces with CH_3OH in the absence or presence of Cp_2Fe^+. The reaction of H–Si(111) with

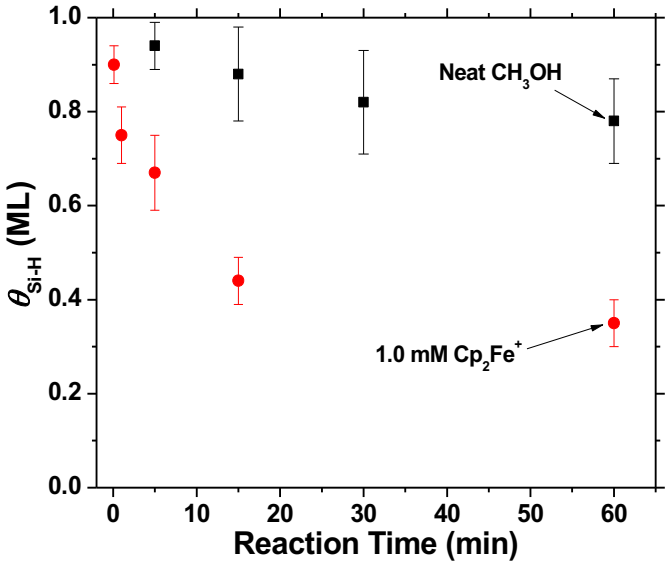

Figure 5.1. Time dependence of the reaction of H–Si(111) with neat CH_3OH and CH_3OH containing 1.0 mM Cp_2Fe^+ in the dark. θ_{Si-H} was determined from TIRS measurements using eq 5.3. Figure courtesy of M. Dasog.

CH_3OH proceeded slowly in the absence of electron acceptors in solution, but increased substantially upon addition of Cp_2Fe^+. This observation agrees with previous results that describe increased reaction rates for the methoxylation of H–Si(111) in CH_3OH solutions that contained Cp_2Fe^+ or $Me_2Cp_2Fe^+$.[18, 21, 68-69]

A substantial difference in the peak area of the Si–H stretching, ν(Si–H), signal was observable between the two reaction conditions after a 5 min reaction time. A greater difference was observed for a 15 min reaction time, but measurable subsurface silicon oxide (SiO_x) was consistently observed after 15 min in the presence of Cp_2Fe^+. Therefore, a 5 min reaction time was chosen as a standard point of comparison in this work.

The reaction of H–Si(111) surfaces with liquid CH_3OH was performed for 5 min in solutions that contained 1.0 mM of the oxidants indicated in Figure 5.2 as well as in

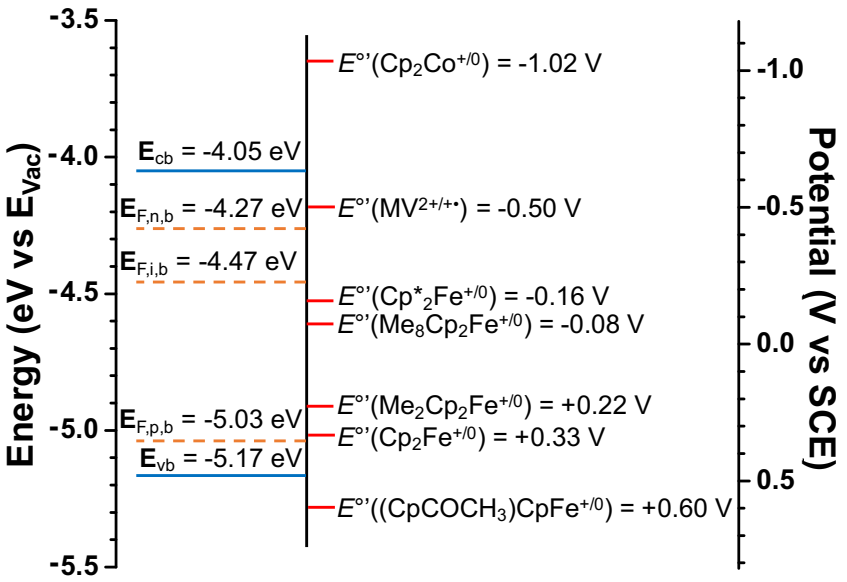

Figure 5.2. Energy diagram showing the relative energy positions vs the vacuum level ($\mathbf{E}_{Vac}$) of the Si valence band maximum ($\mathbf{E}_{vb}$), Si conduction band minimum ($\mathbf{E}_{cb}$), and the calculated bulk Fermi levels (eq 5.1 and eq 5.2) of the intrinsic Si(111) ($\mathbf{E}_{F,i,b}$), n-type Si(111) ($\mathbf{E}_{F,n,b}$), and p-type Si(111) ($\mathbf{E}_{F,p,b}$) used in this work. The measured formal potentials ($E°'$) vs SCE of each oxidant are indicated relative to the Si band positions (SCE = –($\mathbf{E}_{Vac}$ + 4.68)).

neat CH_3OH. The experimentally determined formal potentials, $E°'(A/A^-)$, for each oxidant are indicated relative to the energy positions of the Si valence band, the Si conduction band, and the Fermi levels of the planar Si samples used in this work.[63] The formal potentials of the oxidants spanned the range from below the valence-band maximum to above the conduction-band minimum, allowing for determination of the reactivity of H–Si(111) with CH_3OH over a wide range of oxidizing conditions. Note that only the oxidized species were added to CH_3OH solutions, except in the case of $(CpCOCH_3)CpFe^+$, and the Nernstian solution potentials were thus shifted positive of the measured formal potentals.

Figure 5.3 shows TIRS data for H–Si(111) surfaces after 5 min of exposure to CH_3OH in the presence or absence of the indicated oxidants. The peak positions, shifts, and assignments have been described previously.[21] The highest reactivity, for which the ν(Si–H) peak area (Figure 5.3a) substantially broadened and reduced in intensity compared with the initial peak area, was observed for reactions performed using $(CpCOCH_3)CpFe^+$, Cp_2Fe^+, and $Me_2Cp_2Fe^+$ as oxidants. The activity of these three oxidants is also indicated by the presence of three substantial C–H stretching, $\nu(C–H)_{CH_3}$, peaks (Figure 5.3b) and two broad peaks shown in Figure 5.3c that correspond to C–H symmetric bending, $\delta_s(C–H)_{CH_3}$, and to a complex mode that consists of O–C stretching, ν(O–C), coupled with $–CH_3$ rocking, $\rho(CH_3)$. A broad and low-intensity shoulder on the low energy side of the complex ν(O–C) + $\rho(CH_3)$ was occasionally observed, and corresponds to transverse optical Si–O–Si stretching, $\nu(Si–O–Si)_{TO}$.

The transition from the broad, low-intensity peak observed for reactions performed with $Me_2Cp_2Fe^+$ to the sharp peak observed for reactions performed with $Me_8Cp_2Fe^+$ represents the most evident shift in reaction behavior. The ν(Si–H) peak generally sharpened gradually as $E°'(A/A^–)$ decreased beyond $E°'(Me_8Cp_2Fe^{+/0})$. The overall peak shape for reactions performed with Cp_2Co^+ was comparable to reactions performed in the absence of oxidant.

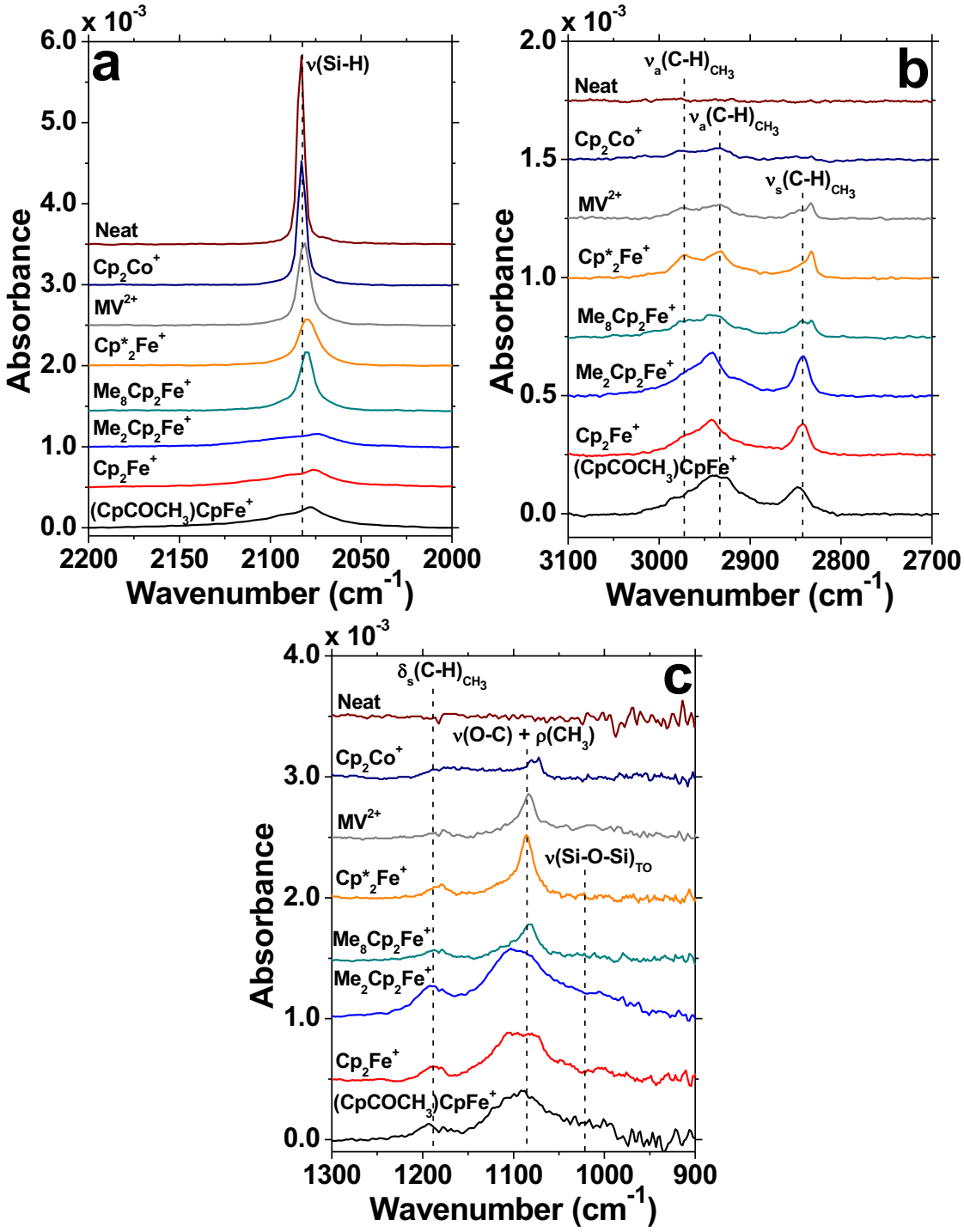

Figure 5.3. TIRS data for intrinsic H–Si(111) surfaces after treatment in neat CH_3OH or CH_3OH containing 1.0 mM of oxidant in the dark for 5 min. The Si–H stretching peak (a), the C–H stretching peaks (b), and the C–H bending and O–C stretching coupled with the CH_3 rocking peaks (c) are shown with the oxidant indicated above each spectrum. The spectra are offset vertically for clarity. The symbols ν, δ, and ρ denote stretching, bending, and rocking motions, respectively.

The intensity and width of the modes associated with the grafting of $–OCH_3$ groups to the H–Si(111) surface presented in Figure 5.3b and Figure 5.3c were greatly reduced for $Me_8Cp_2Fe^+$ and $Cp^*_2Fe^+$ compared with the peak areas observed for more oxidizing species. These spectral features were further weakened for reactions performed in solutions that contained MV^{2+}, and reactions performed in neat CH_3OH or in CH_3OH that contained Cp_2Co^+ yielded nearly undetectable $\nu(C–H)_{CH_3}$, $\delta_s(C–H)_{CH_3}$, or $\nu(O–C)$ + $\rho(CH_3)$ modes. These results indicate that the thermodynamic formal potential of oxidants with $E°'(A/A^–) \leq E°'(Me_8Cp_2Fe^{+/0})$ is not sufficient to efficiently promote oxidative addition of CH_3OH to H–Si(111).

Figure 5.4a presents values of $\theta_{Si–OCH_3}$ determined from TIRS measurements as a function of the oxidizing conditions used for the reaction of H–Si(111) with CH_3OH for intrinsic, n-type, and p-type H–Si(111) samples. The data presented in Figure 5.4a show a relatively constant $\theta_{Si–OCH_3}$ for $(CpCOCH_3)CpFe^+$, Cp_2Fe^+, and $Me_2Cp_2Fe^+$ as the oxidant. A substantial decrease in $\theta_{Si–OCH_3}$ was observed for reactions performed in CH_3OH solutions that contained oxidants having $E°'(A/A^–) \leq E°'(Me_8Cp_2Fe^{+/0})$. This transition, which occurred for $E°'(A/A^–)$ between 0.22 V and –0.08 V vs SCE, is marked in Figure 5.4 by a vertical black dotted line. The general trend indicated that $(CpCOCH_3)CpFe^+$, Cp_2Fe^+, and $Me_2Cp_2Fe^+$ were capable of serving as electron acceptors in the reaction of H–Si(111) with CH_3OH, while $Me_8Cp_2Fe^+$, $Cp^*_2Fe^+$, MV^{2+}, and Cp_2Co^+ were not effective oxidants in driving this reaction.

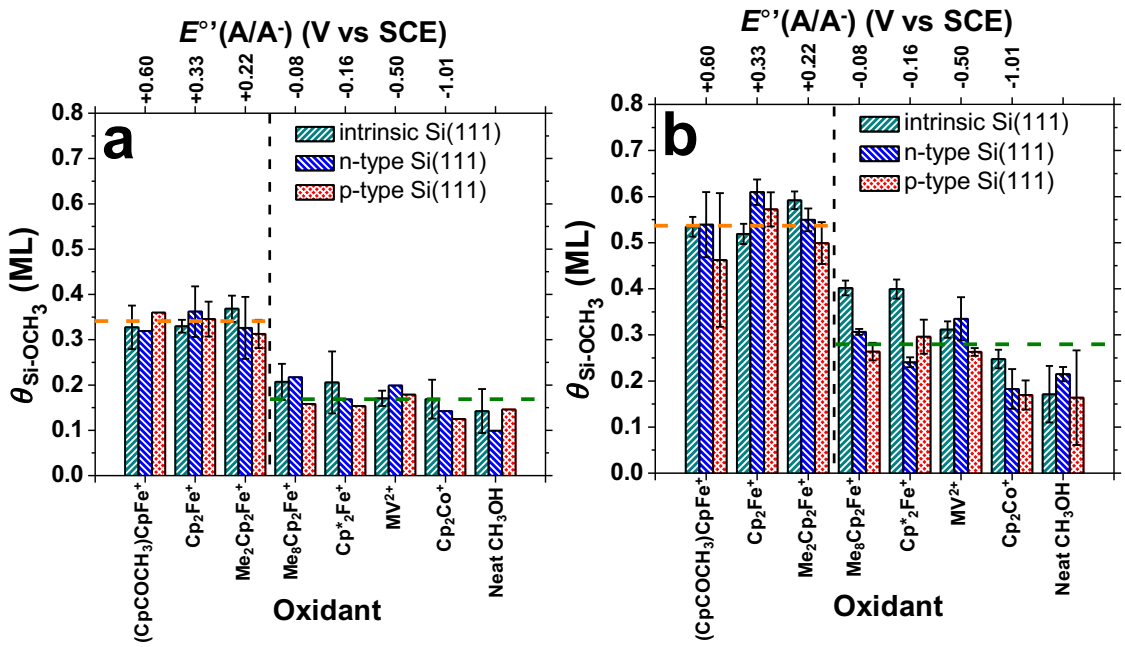

Figure 5.4. Correlation between $\theta_{Si–OCH_3}$ and the oxidizing conditions used in the reaction of H–Si(111) surfaces with CH_3OH in the dark. Reactions were performed for 5 min in neat CH_3OH or CH_3OH containing 1.0 mM of the oxidant species indicated. The experimentally determined formal potentials, $E°'(A/A^-)$, for each oxidant are given above each plot. Panel a gives $\theta_{Si–OCH_3}$ determined by TIRS measurements using eqs 5.1 and 5.2, and panel b gives $\theta_{Si–OCH_3}$ determined by XPS measurements using eq 5.5. The orange and green dotted lines are averages of $\theta_{Si–OCH_3}$ for all samples left and right of the black dotted line, respectively. Error bars represent statistical variation across multiple samples, and data points with no error bars represent single measurements.

Figure 5.4b presents values of $\theta_{Si–OCH_3}$ determined from XPS measurements as a function of the oxidizing conditions used. For all sample types, the values of $\theta_{Si–OCH_3}$ determined by XPS were substantially larger than those determined using TIRS measurements. For reference, the C 1s core level XP spectra for representative H–Si(111) samples after 5 min exposure to CH_3OH solutions is shown in Figure 5.5. Adventitious hydrocarbon species, the majority of which are likely unbound CH_3OH or THF, contributed to the XPS signal ascribable to C bound to O, artificially increasing the value

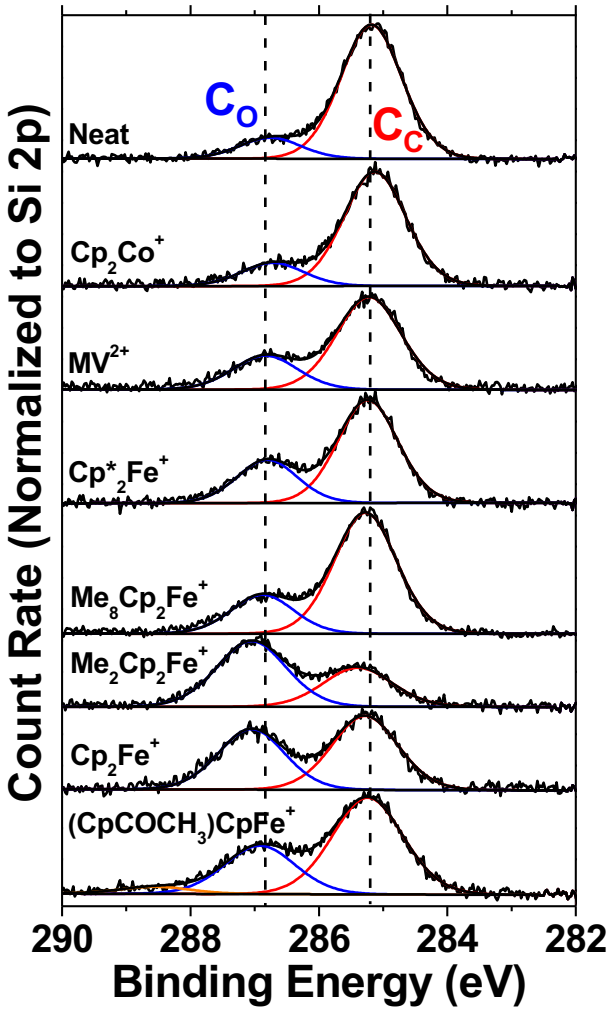

Figure 5.5. XPS data for the C 1s core level of H–Si(111) surfaces after 5 min exposure to neat CH_3OH or CH_3OH solutions containing 1.0 mM of the oxidant indicated above each spectrum. The approximate positions of the C bound to O (C_O) and C bound to C (C_C) peaks are indicated. The C_C peak arises from adventitious hydrocarbon species. The intensity of each spectrum was normalized to the Si 2p core level intensity, and the spectra are offset vertically for clarity.

of $\theta_{Si–OCH_3}$ determined by XPS. The results in Figure 5.4b nevertheless show a large and relatively stable $\theta_{Si–OCH_3}$ for reactions performed in CH_3OH solutions that contained $(CpCOCH_3)CpFe^+$, Cp_2Fe^+, or $Me_2Cp_2Fe^+$ as oxidants, with a marked decrease in $\theta_{Si–OCH_3}$ for reactions performed in CH_3OH solutions that contained $Me_8Cp_2Fe^+$.

Compared with results for TIRS measurements, for oxidants with $E°'(A/A^-) \leq -0.08$ V vs SCE, the overall trend showed that θ_{Si-OCH_3} decreased more gradually as the formal potential of the oxidant in solution became less oxidizing.

Figure 5.6 presents the area under the $\nu(C-H)_{CH_3}$ peaks (3050–2800 cm^{-1}) as a function of the oxidizing conditions used. These data closely parallel the XPS data

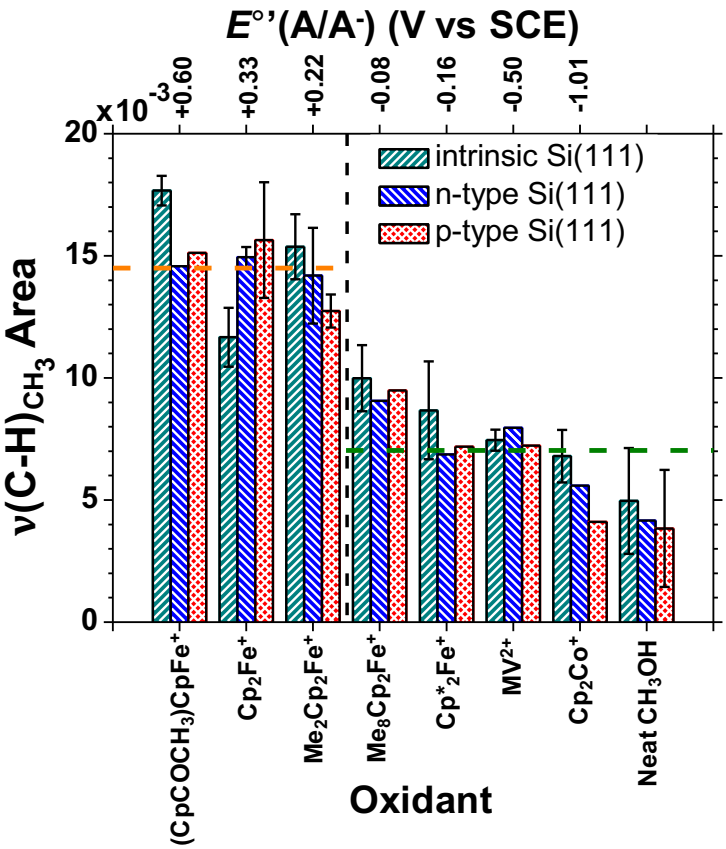

Figure 5.6. Correlation showing the area under the region containing the three $\nu(C-H)_{CH_3}$ peaks (3050–2800 cm^{-1}) as a function of the oxidizing conditions used in the reaction of H–Si(111) surfaces with CH_3OH in the absence of light. Reactions were performed for 5 min in neat CH_3OH or CH_3OH containing 1.0 mM of an oxidant. The experimentally determined formal potentials, $E°'(A/A^-)$, for each oxidant are given above the plot. The orange and green dotted lines are averages of the area under the $\nu(C-H)_{CH_3}$ peaks for all samples left and right of the black dotted line, respectively. Error bars represent statistical variation across multiple samples, and data points with no error bars represent single measurements.

presented in Figure 5.4b, with the largest peak areas observed for reactions performed in CH_3OH solutions that contained $(CpCOCH_3)CpFe^+$, Cp_2Fe^+, and $Me_2Cp_2Fe^+$ as oxidants. Oxidants with $E°'(A/A^-) \leq -0.08$ V vs SCE yielded a decreased $\nu(C–H)_{CH_3}$ peak area compared with the three most oxidizing species. The $\nu(C–H)_{CH_3}$ peak area, like the C 1s photoemission signal, is sensitive to adventitious hydrocarbons, thereby introducing a potentially confounding variable in interpreting the XPS data. Nonetheless, the data indicate a trend showing a gradual decrease in the $\nu(C–H)_{CH3}$ peak area as $E°'(A/A^-)$ decreased, in agreement with the data presented in Figure 4.

Figure 5.7 presents the area under the $\delta_s(C–H)_{CH_3}$ and complex $\nu(C–O) + \rho(CH_3)$ peaks (1250–950 cm^{-1}) as a function of the oxidizing conditions used. The results show a clear difference between oxidants having $E°'(A/A^-) \geq 0.22$ V vs SCE and oxidants with $E°'(A/A^-) \leq -0.08$ V vs SCE. Specifically, a substantial decrease in peak area was apparent between reactions performed in CH_3OH solutions that contained $Me_2Cp_2Fe^+$ relative to reactions in CH_3OH solutions that contained $Me_8Cp_2Fe^+$. The data in Figure 5.7 closely parallel the observed trend in Figure 5.4a.

The TIRS peak area analysis data presented in Figure 5.4a and Figure 5.6 clearly indicate that the oxidant-activated reaction of H–Si(111) surfaces with CH_3OH is not effectively achieved by oxidants having $E°'(A/A^-) \leq E°'(Me_8Cp_2Fe^{+/0})$. Additionally, the data indicate that, in the dark, the reaction of H–Si(111) samples with CH_3OH under the specified conditions is independent of the dopant type and dopant density of the Si(111) substrate.

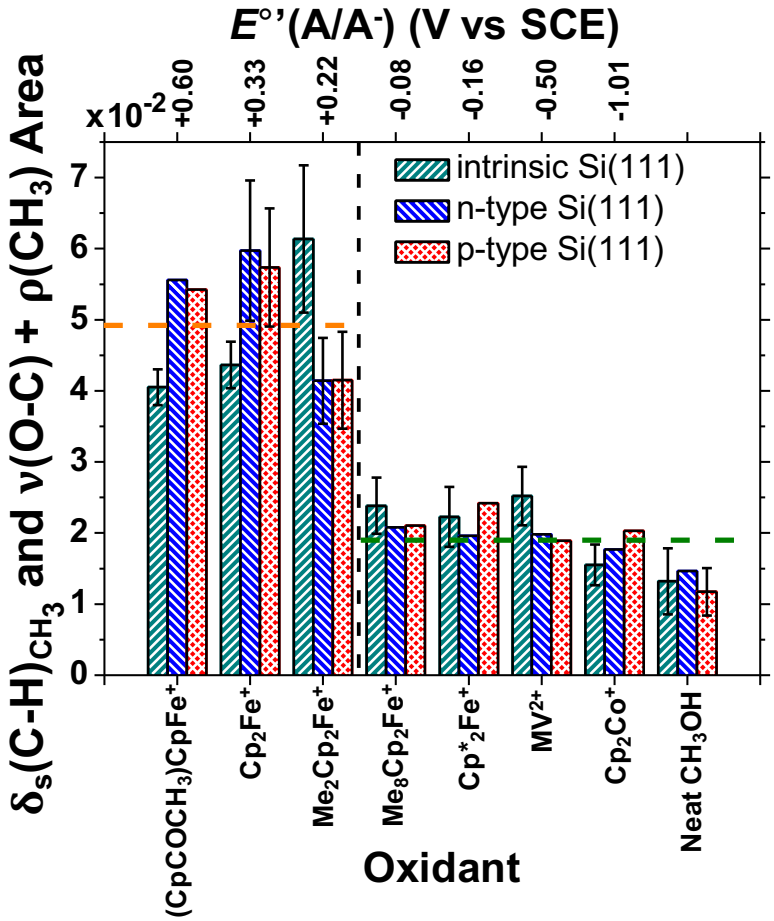

Figure 5.7. Correlation showing the area under the region containing the $\delta_s(C–H)_{CH_3}$ and $\nu(C–O) + \rho(CH_3)$ peaks (1250–950 cm^{-1}) as a function of the oxidizing conditions used in the reaction of H–Si(111) surfaces with CH_3OH in the absence of light. Reactions were performed for 5 min in neat CH_3OH or CH_3OH containing 1.0 mM of an oxidant. The experimentally determined formal potentials, $E°'(A/A^-)$, for each oxidant are given above the plot. The orange and green dotted lines are averages of the area under the $\delta_s(C–H)_{CH_3}$ and $\nu(C–O) + \rho(CH_3)$ peaks for all samples left and right of the black dotted line, respectively. Error bars represent statistical variation across multiple samples, and data points with no error bars represent single measurements.

5.3.2 Reaction of H–Si(111) with CH_3OH Solutions in the Presence of Light

Figure 5.8 shows $\theta_{Si–OCH_3}$ as a function of the oxidizing conditions used for the reaction of H–Si(111) with CH_3OH in the dark or under ambient light. For intrinsic or n-

type H–Si(111) samples in CH_3OH solutions that contained Cp_2Fe^+ or $Me_2Cp_2Fe^+$, $\theta_{Si–OCH_3}$ determined by TIRS measurements after a 5 min reaction in the presence of ambient light increased relative to $\theta_{Si–OCH_3}$ for the same reaction in the dark. For intrinsic or n-type H–Si(111) samples in CH_3OH solutions that contained $Me_8Cp_2Fe^+$, the reaction in ambient light exhibited significantly higher $\theta_{Si–OCH_3}$ compared with the same reaction in the dark, but the level of reactivity was not the same as that observed for CH_3OH solutions that contained Cp_2Fe^+ or $Me_2Cp_2Fe^+$. For solutions that contained $Cp^*_2Fe^+$, MV^{2+}, or Cp_2Co^+, intrinsic or n-type H–Si(111) samples exhibited $\theta_{Si–OCH_3}$ that was comparable to $\theta_{Si–OCH_3}$ observed in the dark. The results observed for p-type H–Si(111) surfaces in the light were not statistically different from the results observed in the dark.

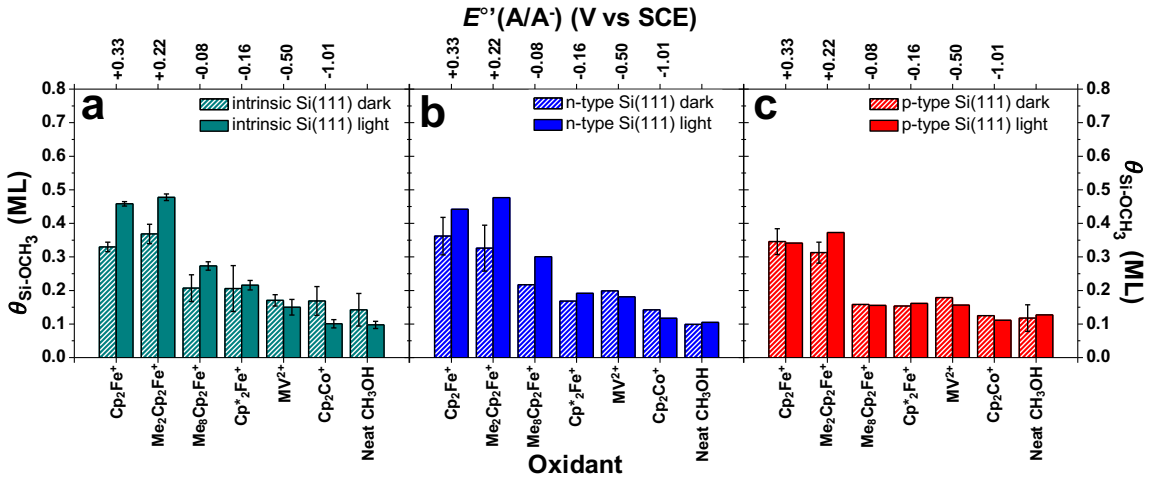

Figure 5.8. Correlation between $\theta_{Si–OCH_3}$ and the oxidizing conditions used in the reaction of (a) intrinsic, (b) n-type, and (c) p-type H–Si(111) surfaces with CH_3OH in the absence (striped) and presence (solid) of ambient light. Reactions were performed for 5 min in neat CH_3OH or CH_3OH containing 1.0 mM of an oxidant. Experimentally determined formal potentials, $E°'(A/A^-)$, for each oxidant are given above each plot. The values for $\theta_{Si–OCH_3}$ were determined by TIRS measurements using eqs 5.1 and 5.2. Error bars represent statistical variation across multiple samples, and data points with no error bars represent single measurements.

The intrinsic samples, so called because of their low dopant density, were very lightly n-doped (Figure 5.2), implying that the valence band states are fully occupied in the absence of illumination. The reactivity observed herein indicates that samples having Fermi levels situated positive of (above) the middle of the band gap, that is, intrinsic or n-type samples, were capable of exhibiting an increased rate of methoxylation of H–Si(111) surfaces in the presence of illumination relative to the rate of methoxylation in the dark.

5.3.3 Analysis of F Content on H–Si(111) Surfaces Reacted in CH_3OH Solutions

XPS detected the presence of F on a number of H–Si(111) samples after reaction with CH_3OH in the presence of an oxidant having a F-based counter ion (BF_4^-). Figure 5.9 presents representative high-resolution XPS data for the F 1s region of an intrinsic H–Si(111) sample exposed to CH_3OH containing $Me_2Cp_2Fe^+BF_4^-$. A photoemission signal at 686.2 eV was ascribed to free F^- and a photoemission signal at 687.4 eV was ascribed to BF_4^-.[70] The data indicate that a significant fraction of BF_4^- counter ion decomposed to yield F^- and BF_3, the latter being removed from the surface during rinsing. No residual Fe was detected from the oxidant on the surface, indicating that the observed F^- and BF_4^- was adsorbed to the surface upon reduction of the $Me_2Cp_2Fe^+$ species by the H–Si(111) surface to give neutral Me_2Cp_2Fe.

The results from analysis of the F 1s photoemission data from eq 5.6 are presented in Figure 5.10. F was observed primarily on samples that were reacted with CH_3OH containing Cp_2Fe^+ or $Me_2Cp_2Fe^+$. XPS did not detect F on surfaces reacted with CH_3OH containing $(CpCOCH_3)CpFe^+$, which was generated in situ prior to use, or

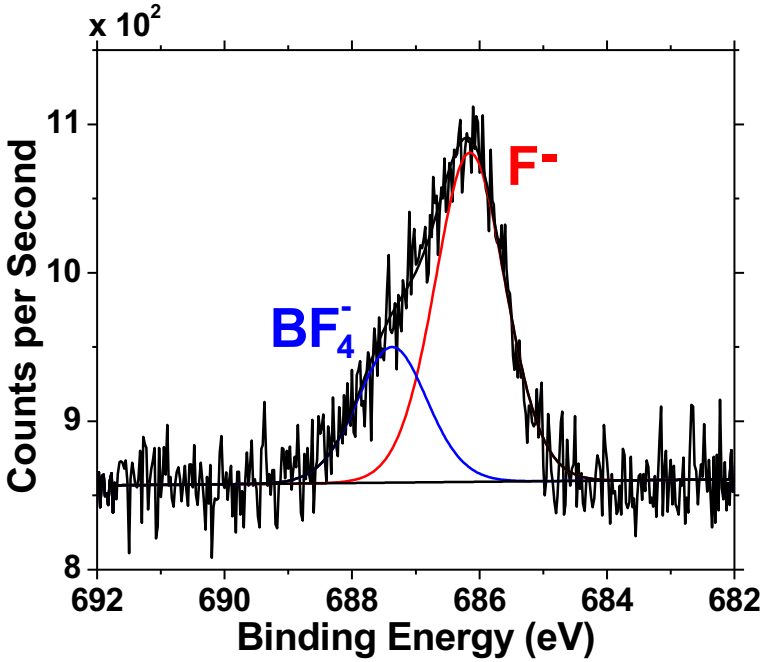

Figure 5.9. High-resolution XPS data for the F 1s region of an intrinsic H–Si(111) sample reacted with CH_3OH containing 1.0 mM $Me_2Cp_2Fe^+BF_4^-$ for 5 min in ambient light. The BF_4^- counter ion provided the source of the F detected.

$Cp_2Co^+PF_6^-$. Samples reacted with CH_3OH solutions containing $MV^{2+}2Cl^-$ did not exhibit detectable Cl by XPS. F was only observed in trace amounts on samples reacted with CH_3OH containing $Me_8Cp_2Fe^+$ or $Cp^*_2Fe^+$, and F was detected more often for these oxidants when the reactions were performed with illumination present. This data indicate that only samples reacted with CH_3OH under conditions that allow for oxidant-mediated methoxylation of the H–Si(111) surface exhibited detectable levels of F on the surface. This provides evidence for the transfer of electrons to Cp_2Fe^+ or $Me_2Cp_2Fe^+$, leaving the BF_4^- counter ion associated with a H^+ from the methoxylation reaction adsorbed to the surface.

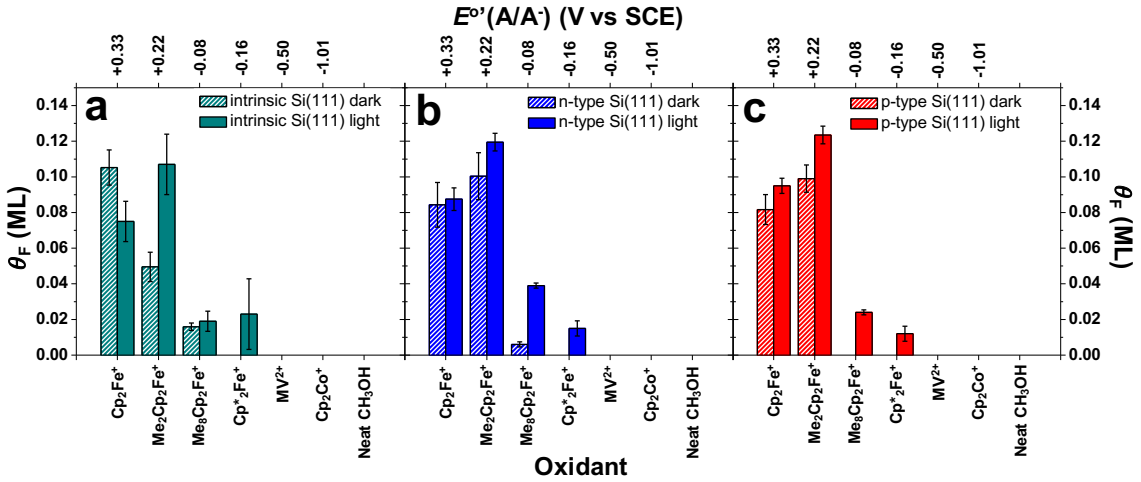

Figure 5.10. Correlation between θ_F and the oxidizing conditions used in the reaction of (a) intrinsic, (b) n-type, and (c) p-type H–Si(111) surfaces with CH_3OH in the absence (striped) and presence (solid) of ambient light. Reactions were performed for 5 min in neat CH_3OH or CH_3OH containing 1.0 mM of an oxidant. Experimentally determined formal potentials, $E^{o'}(A/A^-)$, for each oxidant are given above each plot. The values for θ_F were determined by XPS measurements using eq 5.6.

5.3.4 Potentiostatic Reaction of H–Si(111) with CH_3OH

The reaction of H–Si(111) with CH_3OH was investigated under applied external bias in the dark as well as under illumination. Figure 5.11 presents *J-E* data for n-type and p-type H–Si(111) surfaces in contact with CH_3OH solutions that contained 1.0 M $LiClO_4$ as the supporting electrolyte. In the dark, the methoxylation of n-type H–Si(111) was observed as a gradual increase in current starting near –0.4 V vs SCE, with a peak observed at –0.08 V vs SCE. A gradual decline in current was observed past the peak current, suggesting that the initial rise in current arose from methoxylation of H–Si(111) surfaces. Under illumination, n-type H–Si(111) surfaces showed much higher current density, in addition to a sharp peak centered at –0.17 V vs SCE that is consistently assigned to the methoxylation of H–Si(111) surfaces. At more positive potentials, a rapid

rise in current density was observed beginning at 0 V vs SCE, and was indicative of subsurface oxidation of the Si(111) substrate.

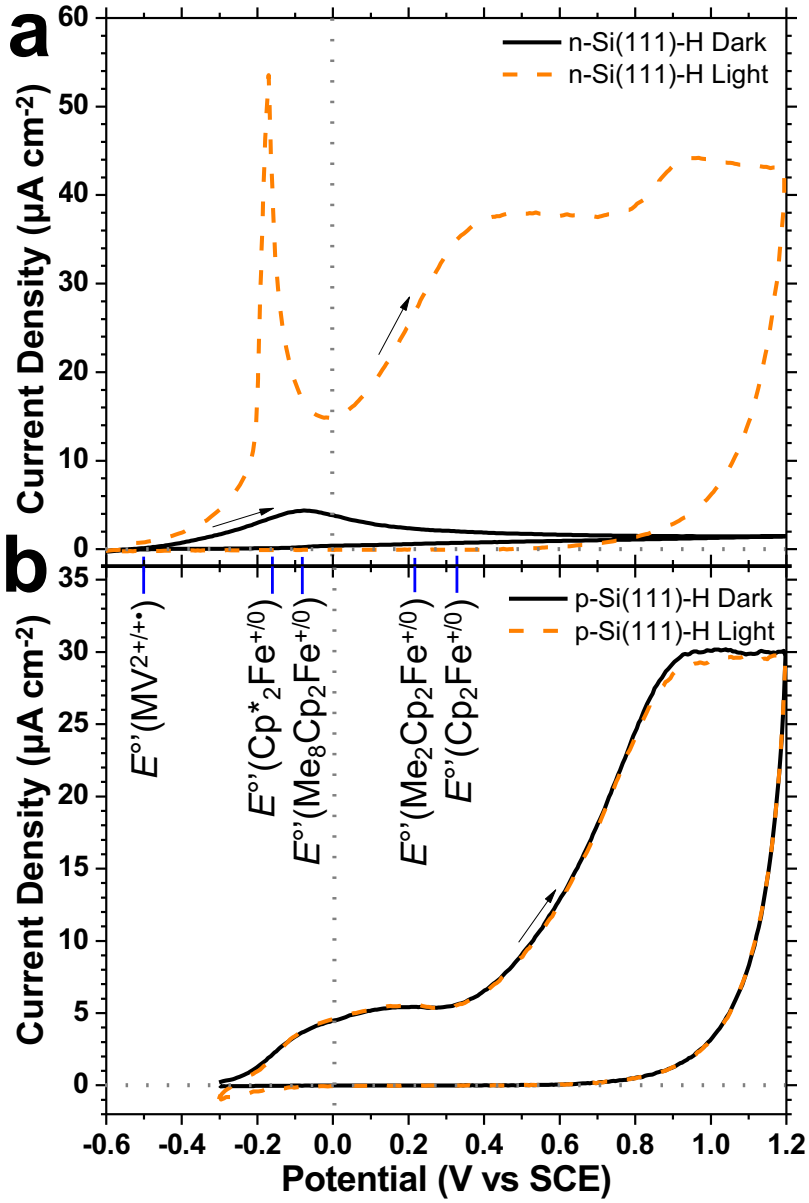

Figure 5.11. *J-E* behavior of (a) n-type and (b) p-type H–Si(111) samples in contact with CH_3OH solutions containing 1.0 M $LiClO_4$ as supporting electrolyte. Data collected in the dark (solid black) and under 10 mW cm^{-2} of simulated solar illumination (dashed orange) are shown. The formal potentials of the oxidants used in this work are indicated by the vertical blue lines at the top of panel b.

For p-type H–Si(111), a gradual increase in current density that is consistently assigned to methoxylation was observed near –0.2 V vs SCE. A distinct peak current due to the methoxylation reaction was not observed directly, as the onset of the subsurface oxidation of the H–Si(111) substrate was observed near +0.4 V vs SCE. The results indicate that the methoxylation of p-type H–Si(111) samples was not sensitive to illumination, as the dark and light curves in Figure 5.11b overlapped substantially. A second sweep of the n-type and p-type electrodes in Figure 5.11 (not shown) was flat through the region ascribed to potentiostatic methoxylation.

Table 5.1 summarizes the quantification of the current passed for the region assigned to the methoxylation of H–Si(111) surfaces. The quantification of $\theta_{Si–OCH_3}$ assumed that 2 electrons were passed for the reaction of each surface site with CH_3OH. The $\theta_{Si–OCH_3}$ resulting from potentiostatic methoxylation of n-type H–Si(111) surfaces in the dark was comparable to $\theta_{Si–OCH_3}$ obtained from potentiostatic methoxylation of p-type H–Si(111) surfaces in the dark as well as under illumination. In contrast, illuminated n-type H–Si(111) surfaces showed significantly greater anodic current that resulted in higher $\theta_{Si–OCH_3}$ compared with samples that were methoxylated in the dark.

Table 5.1. Summary of the Quantification for the Potentiostatic Methoxylation of H–Si(111) Surfaces

Dopant Type	Illumination	Potential Range Quantified (V)[a]	θ_{Si-OCH_3} (ML)[b]	Potential at Half $\theta_{Si-OCH3}$ (V)[c]
n-type	Dark	–0.4 to +0.6	0.22 ± 0.05	0.00 ± 0.07
n-type	10 mW cm^{-2}	–0.3 to 0	0.39 ± 0.07	–0.17 ± 0.05
p-type	Dark	–0.2 to +0.3	0.23 ± 0.06	+0.02 ± 0.04
p-type	10 mW cm^{-2}	–0.2 to +0.3	0.20 ± 0.01	+0.02 ± 0.06

[a]Potential vs SCE. [b]Quantified based on anodic current passed assuming 2 electrons per surface site that reacts with CH_3OH. [c]Potential vs SCE at which half the charge attributed to the methoxylation of the surface was passed.

The potential at which half of the current ascribed to the methoxylation reaction had been passed ($E_{1/2}$) was determined and is given in Table 5.1. The $E_{1/2}$ observed for multiple samples was observed to be the same within error for n-type samples in the dark and p-type samples in the dark or under illumination. For n-type samples under illumination, $E_{1/2}$ was shifted by –0.17 ± 0.05 V compared with n-type samples in the dark, indicating the presence of a photovoltage at the n-Si interface that produced higher anodic current densities and shifted $E_{1/2}$ to more negative potentials.

5.4. DISCUSSION

5.4.1. Kinetic Description and Mechanism of Oxidant-Activated Methoxylation of H–Si(111) Surfaces

The data reported herein indicate that there are potentially two mechanisms by which the methoxylation of H–Si(111) surfaces can occur. Methoxylation in the absence of an oxidant has been previously postulated to occur by an electron rearrangement that yields H_2 and the methoxylated surface site.[21] This mechanism (Scheme 5.1) could

conceivably occur by a mechanism in which two electrons undergo transfer from the Si surface to form a H–H bond, which has an ionization energy (15.4 eV)[71] that places the H–H bond state well below the Si valence band maximum. The oxidant-activated methoxylation process has been proposed (Scheme 5.2) to proceed by two consecutive 1-electron transfers[17-18] that could conceivably result in an increased rate of reaction by allowing for a lower activation energy. The two reaction mechanisms occur simultaneously and are not readily isolated. Because the behavior of the oxidant-activated mechanism was found to be dependent on the strength of the oxidants in solution, this discussion aims to develop a kinetic model that describes the behavior of the oxidant-activated methoxylation mechanism that is consistent with the data reported.

An understanding of the surface electronic states native to the H–Si(111) surface provides a foundation for the oxidant-activated methoxylation mechanism. Ultraviolet photoelectron spectroscopy (UPS) indicates that the electrons in the Si–H σ bond on the H–Si(111) surface lie in an occupied electronic surface state having an energy of ~5 eV below the Si valence-band maximum.[72] The electrons in the Si–H σ bond are therefore not directly accessible to the oxidant species or applied external potentials used in this work. Two-photon photoemission (2PPE) spectroscopy has revealed the presence of an occupied surface resonance on H–Si(111) surfaces in vacuum that is centered ~0.1 eV below the valence-band maximum.[73] Theoretical calculations of the local density of states for H–Si(111) surfaces have additionally identified an occupied electronic state at the $\bar{\Gamma}$ point (center) of the surface Brillouin zone immediately below the valence band maximum.[74-75] Upon contact with CH_3OH, hydrogen bonding between the H–Si(111)

surface and the CH_3OH could conceivably increase the electron density at the Si surface and shift the energy of the surface resonance positive into the band gap. Oxidation of this surface resonance by an oxidant in solution or by an applied external potential could initiate the methoxylation reaction by activating the surface Si towards nucleophilic attack by CH_3OH.

Figure 5.12 presents a schematic of n-type and p-type Si interfaced with solutions containing redox species having a Nernstian solution potential of $E(A/A^-)$ with a corresponding energy of $\mathbf{E}(A/A^-) = -qE(A/A^-)$. The proposed energy position of the surface resonance, corresponding to the formal oxidation potential of the surface Si, when the Si is in contact with CH_3OH is indicated by $\mathbf{E}°'(Si^{+/0})$. The placement of $\mathbf{E}°'(Si^{+/0})$ in the Si band gap is justified by the potentiostatic methoxylation experiments that showed $E_{1/2}$ near 0 V vs SCE. The rate constants for cathodic and anodic charge transfer to and from the valence band are represented as $k_{vb,C}$ and $k_{vb,A}$, respectively, and the rate constants for cathodic and anodic charge transfer from and to the conduction band are represented as $k_{cb,C}$ and $k_{cb,A}$, respectively. Note that, for oxidant-activated methoxylation to occur, cathodic current (loss of an electron from the Si surface to the solution) must dominate the anodic current.

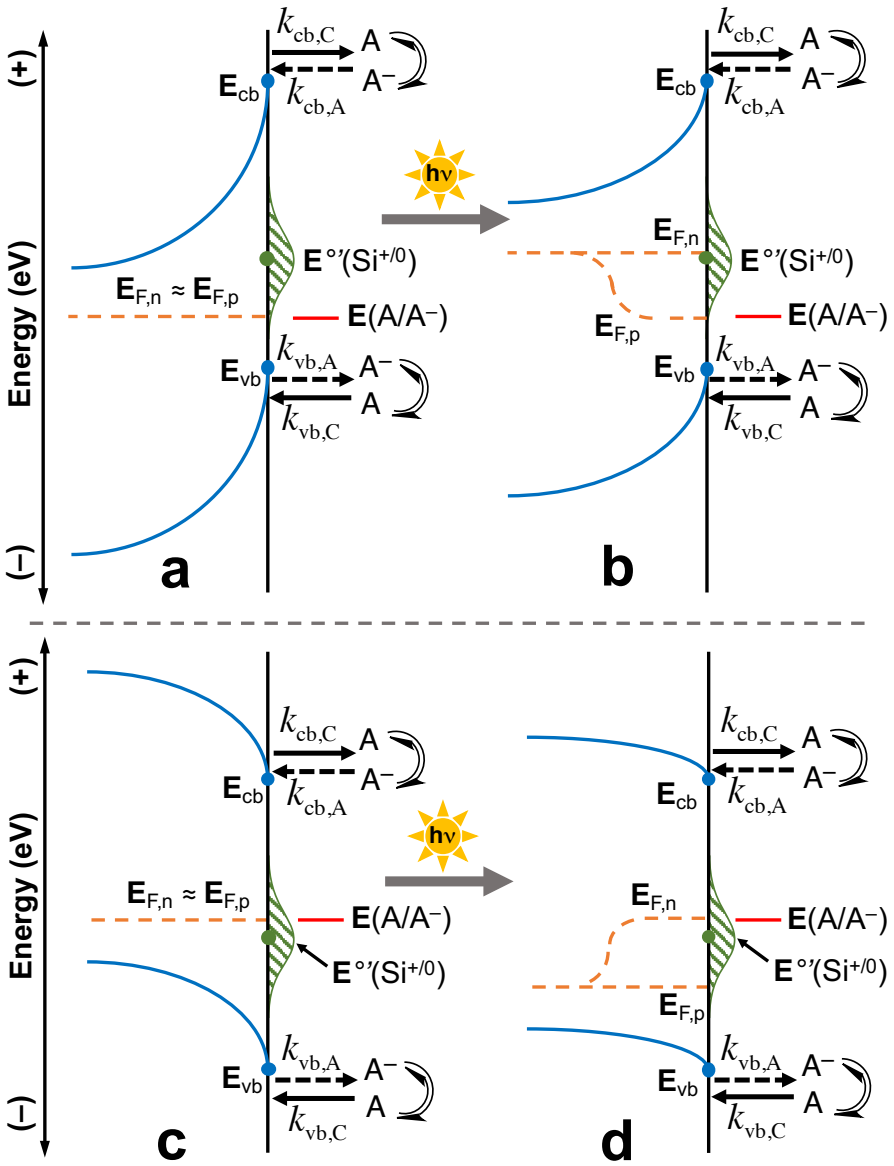

Figure 5.12. Schematic representation of charge transfer across a semiconductor/liquid interface for oxidant-activated methoxylation. The energy positions for the semiconductor valence band ($\mathbf{E}_{vb}$), conduction band ($\mathbf{E}_{cb}$), electron quasi-Fermi level ($\mathbf{E}_{F,n}$), hole quasi-Fermi level ($\mathbf{E}_{F,p}$), the proposed oxidation energy of the surface Si ($\mathbf{E}°'(Si^{+/0})$), and solution energy ($\mathbf{E}(A/A^{-})$) are indicated. The rate constants for cathodic and anodic charge transfer to and from the valence band are $k_{vb,C}$ and $k_{vb,A}$, respectively, and the rate constants for cathodic and anodic charge transfer from and to the conduction band are $k_{cb,C}$ and $k_{cb,A}$, respectively. Solid and dashed arrows indicate cathodic and anodic charge transfer, respectively. Panel a gives the band structure for an n-type contact in the dark, and panel b shows the same contact under illumination. Panel c gives the band structure for a p-type contact in the dark, and panel c shows the same contact under illumination.

The kinetic behavior of the oxidant-activated methoxylation of H–Si(111) surfaces is consistent with the standard kinetic model for charge transfer from a semiconductor to a molecular redox species dissolved in solution. The valence band cathodic current density ($J_{vb,C}$) and anodic current density ($J_{vb,A}$) are described by eqs 5.7 and 5.8, respectively.[76-77]

$$J_{vb,C} = -qk_{vb,C}[A] \qquad (5.7)$$

$$J_{vb,A} = qk_{vb,A}p_s[A^-] \qquad (5.8)$$

Here, q is the unsigned elementary charge of an electron, [A] and [A^-] are the concentrations of the molecular oxidant and reductant, respectively, in solution, and p_s is the concentration of holes in the valence band at the surface. Similarly, the conduction band cathodic current density ($J_{cb,C}$) and anodic current density ($J_{cb,A}$) are described by eqs 5.9 and 5.10, respectively.[76-77]

$$J_{cb,C} = -qk_{cb,C}n_s[A] \qquad (5.9)$$

$$J_{cb,A} = qN_Ak_{cb,A}[A^-] \qquad (5.10)$$

Here, n_s is the concentration of electrons in the conduction band at the surface. The ratios $|J_{vb,C}/J_{vb,A}|$ and $|J_{cb,C}/J_{cb,A}|$ are derived in terms of the quasi-Fermi levels below.

The Nernst equation can be rearranged to yield the relationship given in eq 5.11.

$$\frac{[A]}{[A^-]} = e^{\left(\frac{\mathbf{E}^{\circ\prime}(A/A^-)-\mathbf{E}(A/A^-)}{k_BT}\right)} \qquad (5.11)$$

The formal solution energy is represented as $\mathbf{E}^{\circ\prime}(\mathrm{A/A^-}) = -qE^{\circ\prime}(\mathrm{A/A^-})$, the Nernstian solution energy is represented as $\mathbf{E}(\mathrm{A/A^-}) = -qE(\mathrm{A/A^-})$, and k_B is the Boltzmann constant, and T is the absolute temperature. The ratio of the cathodic to anodic charge transfer rate constants for the valence band and the conduction band are given in eqs 5.12 and 5.13, respectively.[78]

$$\frac{k_{\mathrm{vb,C}}}{k_{\mathrm{vb,A}}} = N_{\mathrm{V}} e^{\left(\frac{\mathbf{E}_{\mathrm{vb}} - \mathbf{E}^{\circ\prime}(\mathrm{A/A^-})}{k_B T}\right)} \qquad (5.12)$$

$$\frac{k_{\mathrm{cb,C}}}{k_{\mathrm{cb,A}}} = \frac{1}{N_{\mathrm{C}}} e^{\left(\frac{\mathbf{E}_{\mathrm{cb}} - \mathbf{E}^{\circ\prime}(\mathrm{A/A^-})}{k_B T}\right)} \qquad (5.13)$$

Here, N_{V} and N_{C} are the effective densities of states of the valence and conduction bands, respectively, $\mathbf{E}_{\mathrm{vb}}$ is the valence band energy, and $\mathbf{E}_{\mathrm{cb}}$ is the conduction band energy. Using eqs 5.11–5.13, the general forms for the ratios $|J_{\mathrm{vb,C}}/J_{\mathrm{vb,A}}| = R_{\mathrm{vb}}$ and $|J_{\mathrm{cb,C}}/J_{\mathrm{cb,A}}| = R_{\mathrm{cb}}$ are given in eqs 5.14 and 5.15, respectively.

$$R_{\mathrm{vb}} = \left|\frac{J_{\mathrm{vb,C}}}{J_{\mathrm{vb,A}}}\right| = \frac{N_{\mathrm{V}}}{p_{\mathrm{s}}} e^{\left(\frac{\mathbf{E}_{\mathrm{vb}} - \mathbf{E}(\mathrm{A/A^-})}{k_B T}\right)} \qquad (5.14)$$

$$R_{\mathrm{cb}} = \left|\frac{J_{\mathrm{cb,C}}}{J_{\mathrm{cb,A}}}\right| = \frac{n_{\mathrm{s}}}{N_{\mathrm{C}}} e^{\left(\frac{\mathbf{E}_{\mathrm{cb}} - \mathbf{E}(\mathrm{A/A^-})}{k_B T}\right)} \qquad (5.15)$$

An increase in R_{vb} or R_{cb} indicates an increase in the cathodic current relative to the anodic current, and $R_{\mathrm{vb}} = R_{\mathrm{cb}} = 1$ occurs at equilibrium.

The hole and electron concentrations at the semiconductor surface are related to the quasi-Fermi level positions according to eqs 5.16 and 5.17, respectively.

$$p_s = N_V e^{\left(\frac{\mathbf{E}_{vb}-\mathbf{E}_{F,p}}{k_B T}\right)} \qquad (5.16)$$

$$n_s = N_C e^{\left(\frac{\mathbf{E}_{F,n}-\mathbf{E}_{cb}}{k_B T}\right)} \qquad (5.17)$$

Substituting eq 5.16 for p_s in eq 5.14 gives R_{vb} in terms of the hole quasi-Fermi level position.

$$R_{vb} = e^{\left(\frac{\mathbf{E}_{F,p}-\mathbf{E}\left(A/A^-\right)}{k_B T}\right)} \qquad (5.18)$$

Similarly, substituting eq 5.17 for n_s in eq 5.15 gives R_{cb} in terms of the electron quasi-Fermi level position.

$$R_{cb} = e^{\left(\frac{\mathbf{E}_{F,n}-\mathbf{E}\left(A/A^-\right)}{k_B T}\right)} \qquad (5.19)$$

For eqs 5.18 and 5.19, equilibrium is reached when $\mathbf{E}_{F,n} = \mathbf{E}_{F,p} = \mathbf{E}(A/A^-)$. The oxidant-activated methoxylation reaction is proposed to initiate when two conditions are met: (1) the net cathodic current (transfer of electrons from the semiconductor to the solution) dominates the anodic current, and (2) the holes in the valence band are sufficiently oxidizing that the valence band can oxidize the surface resonance (i.e. $\mathbf{E}_{F,p} < \mathbf{E}°'(Si^{+/0})$). Eq 5.18 shows that the valence band cathodic current dominates the anodic current ($R_{vb} > 1$) when $\mathbf{E}_{F,p} > \mathbf{E}(A/A^-)$, and eq 5.19 shows that the conduction band cathodic current outweighs the anodic current ($R_{cb} > 1$) when $\mathbf{E}_{F,n} > \mathbf{E}(A/A^-)$.

Figure 5.12a and 5.12c depict an n-type and p-type Si samples, respectively, in the dark in contact with a redox species providing a solution energy in the Si band gap. In both cases, the system is at equilibrium, with no net charge passing in either direction. As

$\mathbf{E}(A/A^-)$ moves more oxidizing and approaches $\mathbf{E}_{vb}$, the capacity of the dopant atoms in the solid to equilibrate the surface Fermi levels with the solution is diminished and $\mathbf{E}_{F,n}$ and $\mathbf{E}_{F,p}$ fall out of equilibrium with $\mathbf{E}(A/A^-)$. With $\mathbf{E}_{F,n}$ and $\mathbf{E}_{F,p} > \mathbf{E}(A/A^-)$, R_{vb} and R_{cb} increase exponentially, and cathodic current dominates the anodic current at the interface. Additionally, with $\mathbf{E}_{F,p}$ falling below $\mathbf{E}°'(Si^{+/0})$, the holes in the valence band are able to oxidize the Si surface and initiate the methoxylation reaction.

In the case of $(CpCOCH_3)CpFe^{+/0}$, the oxidized/reduced ratio was 1:9, yielding a Nernstian solution potential $E((CpCOCH_3)CpFe^{+/0})$ = +0.54 V vs SCE, placing the solution potential positive of (below) the $\mathbf{E}_{vb}$. All other oxidants were present without deliberately added reductant, and the corresponding Nernstian solution potentials were shifted positive of the formal potentials in Figure 5.2. Assuming that the reduced species were present as contaminants with an oxidized/reduced ratio near 1000:1, the Nernstian solution potentials were shifted positive by ~0.2 V. This places $-qE(Me_2Cp_2Fe^{+/0})$, $-qE(Cp_2Fe^{+/0})$, and $-qE((CpCOCH_3)CpFe^{+/0})$ at or below $\mathbf{E}_{vb}$, for which $\mathbf{E}_{F,n}$ and $\mathbf{E}_{F,p} > \mathbf{E}(A/A^-)$, with the less oxidizing species having $\mathbf{E}(A/A^-)$ positive of (above) $\mathbf{E}_{vb}$. As the differences $\mathbf{E}_{F,n} - \mathbf{E}(A/A^-)$ and $\mathbf{E}_{F,p} - \mathbf{E}(A/A^-)$ grow more positive, R_{vb} and R_{cb} increase exponentially, which is consistent with the abrupt change in behavior observed in Figure 5.4. The exponential increase in cathodic current could quickly become limited by diffusion in solution, resulting in the similar rates observed for $Me_2Cp_2Fe^{+/0}$, $Cp_2Fe^{+/0}$, and $CpCOCH_3)CpFe^{+/0}$ The experimental results in the dark presented in Figure 5.4 are consistent with the charge transfer model in Figure 5.12a and 5.12c, where charge transfer equilibrium is maintained for n-type and p-type samples until $\mathbf{E}(A/A^-) \leq \mathbf{E}_{vb}$.

Under illumination, n-type samples exhibit a photovoltage that results from quasi-Fermi level splitting at the interface, as depicted in Figure 5.12b. For a sample with substantial band bending at the interface, n_s is substantially depleted such that illumination pushes the electron quasi-Fermi level positive of $\mathbf{E}(A/A^-)$, while the hole quasi-Fermi level remains equilibrated with $\mathbf{E}(A/A^-)$. For n-type samples, R_{vb} remains at equilibrium, while R_{cb} increases exponentially with the difference $\mathbf{E}_{F,n} - \mathbf{E}(A/A^-)$, allowing cathodic charge transfer to occur from the conduction band to solution. With $R_{cb} > 1$ at illuminated n-type interfaces, oxidant-activated methoxylation can occur at more positive $\mathbf{E}(A/A^-)$ than was observed in the dark, given that $\mathbf{E}_{F,p} < \mathbf{E}°'(Si^{+/0})$, as shown in Figure 5.12b. The increase in the reactivity of illuminated intrinsic and n-type H–Si(111) surfaces toward CH_3OH solutions containing $Me_8Cp_2Fe^+$ compared with the reactivity in the dark (Figure 5.8a and 5.8b) is in agreement with the charge transfer model developed here.

Illuminated p-type samples, which have depleted p_s at the interface, exhibit an a decrease in $\mathbf{E}_{F,p}$ relative to $\mathbf{E}(A/A^-)$, which remains equilibrated with $\mathbf{E}_{F,p}$, as shown in Figure 5.12d. The decrease in $\mathbf{E}_{F,p}$ results in $R_{vb} < 1$, and anodic current dominates in the valence band. This increase in anodic current could yield a reduction in the rate of oxidant-activated methoxylation, though this effect would be masked by the baseline rate of methoxylation that occurs in the absence of any oxidant species. The current in the conduction band remains at equilibrium ($R_{cb} = 1$), indicating that illumination of p-type samples does not result in an increase in the cathodic current necessary to drive the oxidant-activated methoxylation reaction. The data presented in Figure 5.8c are in

agreement with the conclusions of the charge transfer model for p-type samples under illumination because the rate of methoxylation of p-type samples was found to be independent of illumination.

5.4.2. Kinetic Description and Mechanism of the Potentiostatic Methoxylation of H–Si(111) Surfaces

The potentiostatic methoxylation reaction performed in this work was performed in the absence of a well-defined 1-electron acceptor species in solution. The anodic current passed (Figure 5.11) during the methoxylation process is assumed to result in oxidation of the Si lattice. Therefore, all current passed resulted from oxidation or reduction of either the surface of the Si electrode or the CH_3OH in solution. Figure 5.13 depicts the energetics at n-type and p-type surfaces electrically connected to a potentiostat in the dark and under illumination.

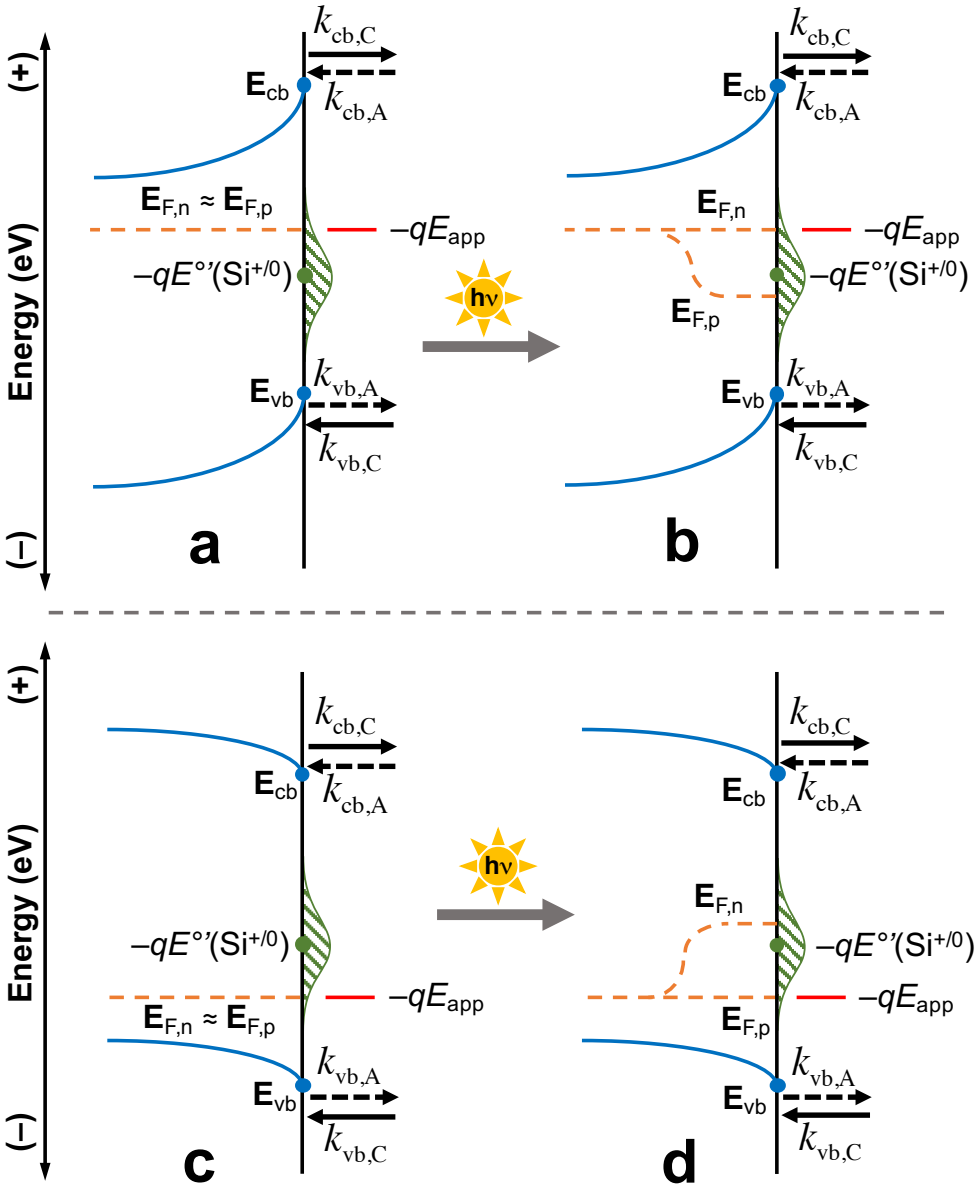

Figure 5.13. Schematic representation of charge transfer across a semiconductor/liquid interface for potentiostatic methoxylation. The energy positions for the semiconductor valence band ($\mathbf{E}_{vb}$), conduction band ($\mathbf{E}_{cb}$), electron quasi-Fermi level ($\mathbf{E}_{F,n}$), hole quasi-Fermi level ($\mathbf{E}_{F,p}$), the proposed oxidation energy of the surface Si ($-qE°'(Si^{+/0})$), and solution energy ($-qE(A/A^{-})$) are indicated. The rate constants for cathodic and anodic charge transfer to and from the valence band are $k_{vb,C}$ and $k_{vb,A}$, respectively, and the rate constants for cathodic and anodic charge transfer from and to the conduction band are $k_{cb,C}$ and $k_{cb,A}$, respectively. Solid and dashed arrows indicate cathodic and anodic charge transfer, respectively. Panel a gives the band structure for an n-type contact in the dark, and panel b shows the same contact under illumination. Panel c gives the band structure for a p-type contact in the dark, and panel c shows the same contact under illumination.

For potentiostatic methoxylation, the electronic states that can accept anodic charge are assumed to be in the Si lattice, and the positions of the quasi-Fermi levels relative to $-qE(Si^{+/0})$ determines the rate of oxidation at the interface. The surface can be oxidized and activated towards reaction with CH_3OH when $\mathbf{E}_{F,n}$ or $\mathbf{E}_{F,p}$ fall at more negative energy than $-qE(Si^{+/0})$. For the potentiostatic reaction, [A] and [A^-] from eqs 5.7–5.10 are fixed at equal concentrations, and so do not factor into the charge transfer equilibrium. Following a derivation similar to that used to arrive at eqs 5.18 and 5.19, the charge transfer equilibrium for potentiostatic methoxylation can be expressed as

$$R_{vb} = e^{\left(\frac{\mathbf{E}_{F,p}-\left(-qE\left(Si^{+/0}\right)\right)}{k_B T}\right)} \qquad (5.20)$$

$$R_{cb} = e^{\left(\frac{\mathbf{E}_{F,n}-\left(-qE\left(Si^{+/0}\right)\right)}{k_B T}\right)} \qquad (5.21)$$

where $-qE(Si^{+/0})$ is the formal oxidation energy for the Si surface, equivalent to $\mathbf{E}(Si^{+/0})$.

The data presented in Figure 5.11 for the dark potentiostatic methoxylation of H–Si(111) surfaces shows that, while the onset potential for potentiostatic methoxylation was more negative for n-type samples than for p-type samples, the potential at which half of the current ascribed to methoxylation had passed ($E_{1/2}$) was near 0 V vs SCE for both dopant densities. Assuming that each surface site can be treated separately, this potential represents the formal oxidation potential of the surface. In order to oxidize the surface, $\mathbf{E}_{F,p}$ or $\mathbf{E}_{F,n}$ must lie lower in energy than $\mathbf{E}(Si^{+/0})$, such that anodic current at the interface dominates the cathodic current.

For n-type and p-type samples in the dark (Figure 5.13a and 5.13c), the band bending at the interface is controlled by the potential applied at the back of the electrode, and the quasi-Fermi levels are assumed to be equilibrated. For $-qE_{app} > \mathbf{E}(Si^{+/0})$, the quasi-Fermi levels are positioned higher in energy than the energy required to oxidize a surface state, and, by eqs 5.20 and 5.21, cathodic current dominates the anodic current from both bands. Here, cathodic current does not affect the rate of methoxylation because the methoxylation reaction is only activated by anodic current. As $-qE_{app}$ decreases, the quasi-Fermi levels at the surface fall low enough in energy that $R_{vb} < 1$ and $R_{cb} < 1$, and the anodic current dominates the cathodic current. Thus, for the conditions $\mathbf{E}_{F,n} < \mathbf{E}(Si^{+/0})$ and $\mathbf{E}_{F,p} < \mathbf{E}(Si^{+/0})$, the methoxylation reaction proceeds at the surface. This model agrees with the data presented in Figure 5.11 because the *J-E* behavior showed an increase in anodic current as $-qE_{app}$ approached $\mathbf{E}(Si^{+/0})$ and both n-type and p-type samples exhibited similar $E_{1/2}$ in the dark.

Illuminated n-type samples (Figure 5.13b) exhibit quasi-Fermi level splitting. Here, $-qE_{app}$ controls the band bending at the interface, and, therefore, is aligned with the majority carrier quasi-Fermi level. Illumination of n-type samples generally results in an increase in p_s, which is dependent on the barrier height, that lowers $\mathbf{E}_{F,p}$ at the interface. Because the methoxylation reaction is activated by anodic current flow at the interface, the decrease in $\mathbf{E}_{F,p}$ upon illumination of n-type interfaces allows the methoxylation reaction to occur at more negative E_{app}. This was observed for illuminated n-type samples as a negative shift in $E_{1/2}$ relative to samples methoxylated in the dark (Table 5.1). Illuminated n-type samples also exhibited nearly double the $\theta_{Si–OCH_3}$ and a significantly

sharper anodic peak ascribed to the methoxylation reaction than samples reacted in dark. These results support the charge transfer model outlined herein, which predicts an increase in anodic current that drives the methoxylation reaction by eq 5.20 ($R_{vb} < 1$) at illuminated n-type interfaces.

The schematic representation of the energetics at the interface of p-type samples is given in Figure 5.13d. Under illumination, n_s increases and pushes $\mathbf{E}_{F,n}$ positive of $\mathbf{E}_{F,p}$, which remains aligned with $-qE_{app}$, resulting in an increase in cathodic current at the interface (R_{cb} increases). The anodic current from the valence band, however, remains the same for a given $-qE_{app}$, resulting in oxidative addition of CH_3OH to the Si surface. The experimental results showed no significant dependence of the potentiostatic methoxylation of p-type H–Si(111) surfaces on the presence of illumination. This suggests that the position of $\mathbf{E}_{F,p}$ relative to $\mathbf{E}(Si^{+/0})$ determines $E_{1/2}$ for the potentiostatic methoxylation reaction. This additionally suggests that an increase in R_{cb} by a more positive $\mathbf{E}_{F,n}$ at illuminated p-type interfaces does not effect the rate of methoxylation, possibly because the electronic states on the surface that are oxidized by $\mathbf{E}_{F,p}$ cannot be further reduced by a more positive $\mathbf{E}_{F,n}$.

5.5. CONCLUSIONS

The reaction of H–Si(111) surfaces with CH_3OH was investigated in the absence or presence of a molecular oxidant and in the absence or presence of illumination. The oxidant-activated methoxylation of H–Si(111) surfaces in the dark proceeded in the presence of oxidants that provided a solution energy, $\mathbf{E}(A/A^-)$, at or below the valence band maximum, $\mathbf{E}_{vb}$. Under ambient illumination, the oxidant-activated methoxylation of

intrinsic and n-type H–Si(111) surfaces exhibited increased reactivity and allowed for oxidants that did not perform oxidant-activated methoxylation in the dark to impart an increased rate of methoxylation in the light. A conventional kinetic framework that predicts an exponential increase in the methoxylation rate as $\mathbf{E}(A/A^{-})$ moves negative of $\mathbf{E}_{vb}$ and the observed behavior under illumination was consistent with the results reported herein. Potentiostatic methoxylation in the dark revealed that the formal oxidation potential of the Si surface, $\mathbf{E}°'(Si^{+/0})$ was approximately 0 V vs SCE, falling near the middle of the band gap. Illumination of n-type H–Si(111) surfaces exposed to CH_3OH under applied external bias resulted in an increase in the anodic current density and a negative shift in $\mathbf{E}_{1/2}$, while p-type H–Si(111) surfaces exposed to CH_3OH under applied external bias were unaffected by the presence of illumination.

The unique reactivity of H–Si(111) surfaces toward CH_3OH not observed for small molecules appears to arise from the narrow band gap of crystalline Si and the capacity of the crystal lattice to form an electric field at the interface that can favor charge transfer in the desired direction. Molecular systems do not have the necessary density of electronic states to perform the oxidant-activated methoxylation reaction for the oxidants used herein. The results presented herein provide a basis for a general mechanistic framework to understand the process by which nucleophiles can undergo reaction with H–Si(111) surfaces in the presence or absence of an oxidant and/or an illumination source.

5.6 REFERENCES

1. Peng, W.; Rupich, S. M.; Shafiq, N.; Gartstein, Y. N.; Malko, A. V.; Chabal, Y. J. Silicon Surface Modification and Characterization for Emergent Photovoltaic Applications Based on Energy Transfer. *Chem. Rev.* **2015**, *115*, 12764-12796.
2. Smith, W. A.; Sharp, I. D.; Strandwitz, N. C.; Bisquert, J. Interfacial Band-Edge Energetics for Solar Fuels Production. *Energy Environ. Sci.* **2015**, *8*, 2851-2862.
3. Buriak, J. M. Illuminating Silicon Surface Hydrosilylation: An Unexpected Plurality of Mechanisms. *Chem. Mater.* **2014**, *26*, 763-772.
4. Huck, L. A.; Buriak, J. M. UV-Initiated Hydrosilylation on Hydrogen-Terminated Silicon (111): Rate Coefficient Increase of Two Orders of Magnitude in the Presence of Aromatic Electron Acceptors. *Langmuir* **2012**, *28*, 16285-16293.
5. G. Robins, E.; P. Stewart, M.; M. Buriak, J. Anodic and Cathodic Electrografting of Alkynes on Porous Silicon. *Chem. Commun.* **1999**, 2479-2480.
6. Ciampi, S.; Böcking, T.; Kilian, K. A.; James, M.; Harper, J. B.; Gooding, J. J. Functionalization of Acetylene-Terminated Monolayers on Si(100) Surfaces: A Click Chemistry Approach. *Langmuir* **2007**, *23*, 9320-9329.
7. Dai, M.; Wang, Y.; Kwon, J.; Halls, M. D.; Chabal, Y. J. Nitrogen Interaction with Hydrogen-Terminated Silicon Surfaces at the Atomic Scale. *Nat. Mater.* **2009**, *8*, 825-830.
8. Tian, F.; Teplyakov, A. V. Silicon Surface Functionalization Targeting Si–N Linkages. *Langmuir* **2013**, *29*, 13-28.
9. Tian, F.; Taber, D. F.; Teplyakov, A. V. –NH– Termination of the Si(111) Surface by Wet Chemistry. *J. Am. Chem. Soc.* **2011**, *133*, 20769-20777.

10. Chopra, T. P.; Longo, R. C.; Cho, K.; Chabal, Y. J. Ammonia Modification of Oxide-Free Si(111) Surfaces. *Surf. Sci.* **2016**, *650*, 285-294.

11. Chopra, T. P.; Longo, R. C.; Cho, K.; Halls, M. D.; Thissen, P.; Chabal, Y. J. Ethylenediamine Grafting on Oxide-Free H-, 1/3 ML F-, and Cl-Terminated Si(111) Surfaces. *Chem. Mater.* **2015**, *27*, 6268-6281.

12. Buriak, J. M.; Sikder, M. D. H. From Molecules to Surfaces: Radical-Based Mechanisms of Si–S and Si–Se Bond Formation on Silicon. *J. Am. Chem. Soc.* **2015**, *137*, 9730-9738.

13. Hu, M.; Liu, F.; Buriak, J. M. Expanding the Repertoire of Molecular Linkages to Silicon: Si–S, Si–Se, and Si–Te Bonds. *ACS Appl. Mater. Inter.* **2016**, *8*, 11091-11099.

14. Yamada, T.; Shirasaka, K.; Noto, M.; Kato, H. S.; Kawai, M. Adsorption of Unsaturated Hydrocarbon Moieties on H:Si(111) by Grignard Reaction. *J. Phys. Chem. B* **2006**, *110*, 7357-7366.

15. Boukherroub, R.; Morin, S.; Bensebaa, F.; Wayner, D. D. M. New Synthetic Routes to Alkyl Monolayers on the Si(111) Surface. *Langmuir* **1999**, *15*, 3831-3835.

16. Cleland, G.; Horrocks, B. R.; Houlton, A. Direct Functionalization of Silicon via the Self-Assembly of Alcohols. *J. Chem. Soc., Faraday Trans.* **1995**, *91*, 4001-4003.

17. Haber, J. A.; Lauermann, I.; Michalak, D.; Vaid, T. P.; Lewis, N. S. Electrochemical and Electrical Behavior of (111)-Oriented Si Surfaces Alkoxylated through Oxidative Activation of Si−H Bonds. *J. Phys. Chem. B* **2000**, *104*, 9947-9950.

18. Haber, J. A.; Lewis, N. S. Infrared and X-ray Photoelectron Spectroscopic Studies of the Reactions of Hydrogen-Terminated Crystalline Si(111) and Si(100) Surfaces with Br_2, I_2, and Ferrocenium in Alcohol Solvents. *J. Phys. Chem. B* **2002**, *106*, 3639-3656.

19. Michalak, D. J.; Amy, S. R.; Aureau, D.; Dai, M.; Esteve, A.; Chabal, Y. J. Nanopatterning Si(111) Surfaces as a Selective Surface-Chemistry Route. *Nat. Mater.* **2010**, *9*, 266-271.

20. Michalak, D. J.; Amy, S. R.; Estève, A.; Chabal, Y. J. Investigation of the Chemical Purity of Silicon Surfaces Reacted with Liquid Methanol. *J. Phys. Chem. C* **2008**, *112*, 11907-11919.

21. Michalak, D. J.; Rivillon, S.; Chabal, Y. J.; Estève, A.; Lewis, N. S. Infrared Spectroscopic Investigation of the Reaction of Hydrogen-Terminated, (111)-Oriented, Silicon Surfaces with Liquid Methanol. *J. Phys. Chem. B* **2006**, *110*, 20426-20434.

22. Dusciac, D.; Chazalviel, J.-N.; Ozanam, F.; Allongue, P.; de Villeneuve, C. H. Thermal Stability of Alkoxy Monolayers Grafted on Si(111). *Surf. Sci.* **2007**, *601*, 3961-3964.

23. Boukherroub, R.; Morin, S.; Sharpe, P.; Wayner, D. D. M.; Allongue, P. Insights into the Formation Mechanisms of Si−OR Monolayers from the Thermal Reactions of Alcohols and Aldehydes with Si(111)−H. *Langmuir* **2000**, *16*, 7429-7434.

24. Thissen, P.; Fuchs, E.; Roodenko, K.; Peixoto, T.; Batchelor, B.; Smith, D.; Schmidt, W. G.; Chabal, Y. Nanopatterning on H-Terminated Si(111) Explained as Dynamic Equilibrium of the Chemical Reaction with Methanol. *J. Phys. Chem. C* **2015**, *119*, 16947-16953.

25. Khung, Y. L.; Ngalim, S. H.; Meda, L.; Narducci, D. Preferential Formation of Si–O–C over Si–C Linkage upon Thermal Grafting on Hydrogen-Terminated Silicon (111). *Chemistry – A European Journal* **2014**, *20*, 15151-15158.

26. Perrine, K. A.; Lin, J.-M.; Teplyakov, A. V. Controlling the Formation of Metallic Nanoparticles on Functionalized Silicon Surfaces. *J. Phys. Chem. C* **2012**, *116*, 14431-14444.

27. Aureau, D.; Varin, Y.; Roodenko, K.; Seitz, O.; Pluchery, O.; Chabal, Y. J. Controlled Deposition of Gold Nanoparticles on Well-Defined Organic Monolayer Grafted on Silicon Surfaces. *J. Phys. Chem. C* **2010**, *114*, 14180-14186.

28. Maldonado, S.; Knapp, D.; Lewis, N. S. Near-Ideal Photodiodes from Sintered Gold Nanoparticle Films on Methyl-Terminated Si(111) Surfaces. *J. Am. Chem. Soc.* **2008**, *130*, 3300-3301.

29. Nguyen, H. M.; Seitz, O.; Aureau, D.; Sra, A.; Nijem, N.; Gartstein, Y. N.; Chabal, Y. J.; Malko, A. V. Spectroscopic Evidence for Nonradiative Energy Transfer between Colloidal CdSe/ZnS Nanocrystals and Functionalized Silicon Substrates. *Appl. Phys. Lett.* **2011**, *98*, 161904.

30. Khatri, O. P.; Ichii, T.; Murase, K.; Sugimura, H. UV Induced Covalent Assembly of Gold Nanoparticles in Linear Patterns on Oxide Free Silicon Surface. *J. Mater. Chem.* **2012**, *22*, 16546-16551.

31. Caillard, L.; Seitz, O.; Campbell, P. M.; Doherty, R. P.; Lamic-Humblot, A.-F.; Lacaze, E.; Chabal, Y. J.; Pluchery, O. Gold Nanoparticles on Oxide-Free Silicon–Molecule Interface for Single Electron Transport. *Langmuir* **2013**, *29*, 5066-5073.

32. O'Leary, L. E.; Strandwitz, N. C.; Roske, C. W.; Pyo, S.; Brunschwig, B. S.; Lewis, N. S. Use of Mixed CH_3–/$HC(O)CH_2CH_2$–Si(111) Functionality to Control Interfacial Chemical and Electronic Properties During the Atomic-Layer Deposition of Ultrathin Oxides on Si(111). *J. Phys. Chem. Lett.* **2015**, *6*, 722-726.

33. Li, M.; Dai, M.; Chabal, Y. J. Atomic Layer Deposition of Aluminum Oxide on Carboxylic Acid-Terminated Self-Assembled Monolayers. *Langmuir* **2009**, *25*, 1911-1914.

34. Peng, W.; Seitz, O.; Chapman, R. A.; Vogel, E. M.; Chabal, Y. J. Probing the Intrinsic Electrical Properties of Thin Organic Layers/Semiconductor Interfaces using an Atomic-Layer-Deposited Al_2O_3 Protective Layer. *Appl. Phys. Lett.* **2012**, *101*, 051605.

35. Peng, W.; DeBenedetti, W. J. I.; Kim, S.; Hines, M. A.; Chabal, Y. J. Lowering the Density of Electronic Defects on Organic-Functionalized Si(100) Surfaces. *Appl. Phys. Lett.* **2014**, *104*, 241601.

36. Bruce, J. P.; Oliver, D. R.; Lewis, N. S.; Freund, M. S. Electrical Characteristics of the Junction between PEDOT:PSS and Thiophene-Functionalized Silicon Microwires. *ACS Appl. Mater. Inter.* **2015**, *7*, 27160-27166.

37. Giesbrecht, P. K.; Bruce, J. P.; Freund, M. S. Electric and Photoelectric Properties of 3,4–Ethylenedioxythiophene-Functionalized n-Si/PEDOT:PSS Junctions. *ChemSusChem* **2016**, *9*, 109-117.

38. Sailor, M. J.; Klavetter, F. L.; Grubbs, R. H.; Lewis, N. S. Electronic Properties of Junctions between Silicon and Organic Conducting Polymers. *Nature* **1990**, *346*, 155-157.

39. Gallant, B. M.; Gu, X. W.; Chen, D. Z.; Greer, J. R.; Lewis, N. S. Tailoring of Interfacial Mechanical Shear Strength by Surface Chemical Modification of Silicon Microwires Embedded in Nafion Membranes. *ACS Nano* **2015**, *9*, 5143-5153.

40. Zhang, F.; Liu, D.; Zhang, Y.; Wei, H.; Song, T.; Sun, B. Methyl/Allyl Monolayer on Silicon: Efficient Surface Passivation for Silicon-Conjugated Polymer Hybrid Solar Cell. *ACS Appl. Mater. Inter.* **2013**, *5*, 4678-4684.

41. Cho, C. J.; O'Leary, L.; Lewis, N. S.; Greer, J. R. In Situ Nanomechanical Measurements of Interfacial Strength in Membrane-Embedded Chemically Functionalized Si Microwires for Flexible Solar Cells. *Nano Lett.* **2012**, *12*, 3296-3301.

42. Fabre, B. Functionalization of Oxide-Free Silicon Surfaces with Redox-Active Assemblies. *Chem. Rev.* **2016**, *116*, 4808-4849.

43. Lattimer, J. R. C.; Blakemore, J. D.; Sattler, W.; Gul, S.; Chatterjee, R.; Yachandra, V. K.; Yano, J.; Brunschwig, B. S.; Lewis, N. S.; Gray, H. B. Assembly, Characterization, and Electrochemical Properties of Immobilized Metal Bipyridyl Complexes on Silicon(111) Surfaces. *Dalton Trans.* **2014**, *43*, 15004-15012.

44. Lattimer, J. R. C.; Brunschwig, B. S.; Lewis, N. S.; Gray, H. B. Redox Properties of Mixed Methyl/Vinylferrocenyl Monolayers on Si(111) Surfaces. *J. Phys. Chem. C* **2013**, *117*, 27012-27022.

45. Kang, O. S.; Bruce, J. P.; Herbert, D. E.; Freund, M. S. Covalent Attachment of Ferrocene to Silicon Microwire Arrays. *ACS Appl. Mater. Inter.* **2015**, *7*, 26959-26967.

46. O'Leary, L. E.; Rose, M. J.; Ding, T. X.; Johansson, E.; Brunschwig, B. S.; Lewis, N. S. Heck Coupling of Olefins to Mixed Methyl/Thienyl Monolayers on Si(111) Surfaces. *J. Am. Chem. Soc.* **2013**, *135*, 10081-10090.

47. Yzambart, G.; Fabre, B.; Roisnel, T.; Dorcet, V.; Ababou-Girard, S.; Meriadec, C.; Lorcy, D. Assembly of Platinum Diimine Dithiolate Complexes onto Hydrogen-Terminated Silicon Surfaces. *Organometallics* **2014**, *33*, 4766-4776.

48. Seo, J.; Pekarek, R. T.; Rose, M. J. Photoelectrochemical Operation of a Surface-Bound, Nickel-Phosphine H_2 Evolution Catalyst on p-Si(111): A Molecular Semiconductor|Catalyst Construct. *Chem. Commun.* **2015**, *51*, 13264-13267.

49. Fabre, B.; Cordier, S.; Molard, Y.; Perrin, C.; Ababou-Girard, S.; Godet, C. Electrochemical and Charge Transport Behavior of Molybdenum-Based Metallic Cluster Layers Immobilized on Modified n- and p-Type Si(111) Surfaces. *J. Phys. Chem. C* **2009**, *113*, 17437-17446.

50. Ciampi, S.; Luais, E.; James, M.; Choudhury, M. H.; Darwish, N. A.; Gooding, J. J. The Rapid Formation of Functional Monolayers on Silicon under Mild Conditions. *Phys. Chem. Chem. Phys.* **2014**, *16*, 8003-8011.

51. Sun, Q.-Y.; de Smet, L. C. P. M.; van Lagen, B.; Giesbers, M.; Thüne, P. C.; van Engelenburg, J.; de Wolf, F. A.; Zuilhof, H.; Sudhölter, E. J. R. Covalently Attached Monolayers on Crystalline Hydrogen-Terminated Silicon: Extremely Mild Attachment by Visible Light. *J. Am. Chem. Soc.* **2005**, *127*, 2514-2523.

52. Wayner, D. D. M.; Wolkow, R. A. Organic Modification of Hydrogen Terminated Silicon Surfaces. *Journal of the Chemical Society, Perkin Transactions 2* **2002**, 23-34.

53. Rosenbluth, M. L.; Lieber, C. M.; Lewis, N. S. 630-mV Open Circuit Voltage, 12% Efficient n-Si Liquid Junction. *Appl. Phys. Lett.* **1984**, *45*, 423-425.

54. Gibbons, J. F.; Cogan, G. W.; Gronet, C. M.; Lewis, N. S. A 14% efficient nonaqueous semiconductor/liquid junction solar cell. *Appl. Phys. Lett.* **1984**, *45*, 1095-1097.

55. Michalak, D. J.; Lewis, N. S. Use of Near-Surface Channel Conductance and Differential Capacitance versus Potential Measurements to Correlate Inversion Layer

Formation with Low Effective Surface Recombination Velocities at n-Si/Liquid Contacts. *Appl. Phys. Lett.* **2002**, *80*, 4458-4460.

56. Gstrein, F.; Michalak, D. J.; Royea, W. J.; Lewis, N. S. Effects of Interfacial Energetics on the Effective Surface Recombination Velocity of Si/Liquid Contacts. *J. Phys. Chem. B* **2002**, *106*, 2950-2961.
57. Royea, W. J.; Michalak, D. J.; Lewis, N. S. Role of Inversion Layer Formation in Producing Low Effective Surface Recombination Velocities at Si/lLiquid Contacts. *Appl. Phys. Lett.* **2000**, *77*, 2566-2568.
58. Chazalviel, J. N. Surface Methoxylation as the Key Factor for the Good Performance of n-Si/Methanol Photoelectrochemical Cells. *Journal of Electroanalytical Chemistry and Interfacial Electrochemistry* **1987**, *233*, 37-48.
59. Rijksen, B.; van Lagen, B.; Zuilhof, H. Mimicking the Silicon Surface: Reactivity of Silyl Radical Cations toward Nucleophiles. *J. Am. Chem. Soc.* **2011**, *133*, 4998-5008.
60. Giese, B.; Dickhaut, J.; Chatgilialoglu, C., Tris(trimethylsilyl)silane. In *Encyclopedia of Reagents for Organic Synthesis*, John Wiley & Sons, Ltd: 2001.
61. Kim, N. Y.; Laibinis, P. E. Thermal Derivatization of Porous Silicon with Alcohols. *J. Am. Chem. Soc.* **1997**, *119*, 2297-2298.
62. Skibinski, E. S.; DeBenedetti, W. J. I.; Rupich, S. M.; Chabal, Y. J.; Hines, M. A. Frustrated Etching during H/Si(111) Methoxylation Produces Fissured Fluorinated Surfaces, Whereas Direct Fluorination Preserves the Atomically Flat Morphology. *J. Phys. Chem. C* **2015**, *119*, 26029-26037.
63. Hunger, R.; Fritsche, R.; Jaeckel, B.; Jaegermann, W.; Webb, L. J.; Lewis, N. S. Chemical and Electronic Characterization of Methyl-Terminated Si(111) Surfaces by

High-Resolution Synchrotron Photoelectron Spectroscopy. *Phys. Rev. B* **2005**, *72*, 045317.

64. Hendrickson, D. N.; Sohn, Y. S.; Gray, H. B. Magnetic Susceptibility Study of Various Ferricenium and Iron(III) Dicarbollide Compounds. *Inorg. Chem.* **1971**, *10*, 1559-1563.
65. Grimm, R. L.; Bierman, M. J.; O'Leary, L. E.; Strandwitz, N. C.; Brunschwig, B. S.; Lewis, N. S. Comparison of the Photoelectrochemical Behavior of H-Terminated and Methyl-Terminated Si(111) Surfaces in Contact with a Series of One-Electron, Outer-Sphere Redox Couples in CH_3CN. *J. Phys. Chem. C* **2012**, *116*, 23569-23576.
66. Plymale, N. T.; Kim, Y.-G.; Soriaga, M. P.; Brunschwig, B. S.; Lewis, N. S. Synthesis, Characterization, and Reactivity of Ethynyl- and Propynyl-Terminated Si(111) Surfaces. *J. Phys. Chem. C* **2015**, *119*, 19847-19862.
67. Plymale, N. T.; Ramachandran, A. A.; Lim, A.; Brunschwig, B. S.; Lewis, N. S. Control of the Band-Edge Positions of Crystalline Si(111) by Surface Functionalization with 3,4,5-Trifluorophenylacetylenyl Moieties. *J. Phys. Chem. C* **2016**, *120*, 14157-14169.
68. Pomykal, K. E.; Fajardo, A. M.; Lewis, N. S. Stability of n-Si/CH_3OH Contacts as a Function of the Reorganization Energy of the Electron Donor. *J. Phys. Chem.* **1995**, *99*, 8302-8310.
69. Shreve, G. A.; Karp, C. D.; Pomykal, K. E.; Lewis, N. S. Limits on the Corrosion Rate of Si Surfaces in Contact with CH_3OH-Ferrocene$^{+/0}$ and CH_3OH-1,1'-Dimethylferrocene$^{+/0}$ Solutions. *J. Phys. Chem.* **1995**, *99*, 5575-5580.
70. Moulder, J. F.; Stickle, W. F.; Sobol, P. E.; Bomen, K. D. *Handbook of X-ray Photoelectron Spectroscopy: A Reference Book of Standard Spectra for Identification*

and Interpretation of XPS Data; Physical Electronics USA, Inc.: Chanhassen, Minnesota, 1995.

71. Price, W. C.; Harris, P. V.; Passmore, T. R. The Ionization and Dissociation Energies of Molecules and Radicals. *J. Quant. Spectrosc. Radiat. Transfer* **1962**, *2*, 327-333.
72. Hideyuki, Y.; Kazuyuki, M.; Shin-ichiro, A.; Hiroyuki, S.; Satoshi, K.; Yasushi, A.; Koji , K. O.; Shinji, H.; Yoshiya, H.; Nobuo, U. Surface States of Hydrogen-Terminated Si(111) by Metastable Atom Electron Spectroscopy and Angle-Resolved Ultraviolet Photoelectron Spectroscopy. *Japanese Journal of Applied Physics* **2000**, *39*, 1706.
73. Nakamura, T.; Miyajima, K.; Hirata, N.; Matsumoto, T.; Morikawa, Y.; Tada, H.; Nakajima, A. Electronic Structure of Hydrogen-Terminated Silicon Surfaces [H–Si(111)] Studied by Two-Photon Photoemission. *Appl. Phys. A* **2010**, *98*, 735-743.
74. Blase, X.; Zhu, X.; Louie, S. G. Self-Energy Effects on the Surface-State Energies of H–Si(111)1x1. *Phys. Rev. B* **1994**, *49*, 4973-4980.
75. Li, Y.; Galli, G. Electronic and Spectroscopic Properties of the Hydrogen-Terminated Si(111) Surface from *ab initio* Calculations. *Phys. Rev. B* **2010**, *82*, 045321.
76. Kumar, A.; Santangelo, P. G.; Lewis, N. S. Electrolysis of Water at Strontium Titanate ($SrTiO_3$) Photoelectrodes: Distinguishing between the Statistical and Stochastic Formalisms for Electron-Transfer Processes in Fuel-Forming Photoelectrochemical Systems. *J. Phys. Chem.* **1992**, *96*, 834-842.
77. Lewis, N. S. An Analysis of Charge Transfer Rate Constants for Semiconductor/Liquid Interfaces. *Annu. Rev. Phys. Chem.* **1991**, *42*, 543-580.

78. Shreve, G. A.; Lewis, N. S. An Analytical Description of the Consequences of Abandoning the Principles of Detailed Balance and Microscopic Reversibility in Semiconductor Photoelectrochemistry. *J. Electrochem. Soc.* **1995**, *142*, 112-119.